

Prioritizing Locations for Distributed Generation: From Cities to Rooftops

Group 6

Jiachen Wei (20695056)

Yunhong Tian (20747876)

Zhihao Wang (20695562)

University of Waterloo

GEOG 471 Remote Sensing Project (Winter 2018)

Dr. Richard Kelly

Friday April 6, 2018

Table of Contents

Chapter 1. Introduction	1
1.1 Motivation.....	1
1.2 Research Objectives.....	2
1.3 Study Area	3
1.4 Roles of Project Members.....	5
1.5 Outlines	5
Chapter 2. Background	6
2.1. Air Pollution.....	6
2.1.1 Dark Target Method.....	7
2.1.2 Deep Blue Algorithm.....	9
2.2. Land Surface Temperature.....	9
2.2.1 Single Channel Method.....	10
2.2.2 Split Window Method.....	12
2.2.3 Limitations	14
2.3. Topographic Factors for Rooftop Photovoltaic Installation	16
2.3.1 Area.....	17
2.3.2 Shading	18
2.3.3 Aspect	18
2.3.4 Slope	20
2.3.5 Rooftop Structures	21
2.3.5.1 Global Corrective Factor.....	21
2.2.5.2 Digitization	21
2.2.5.3 LiDAR.....	22

Chapter 3. Methodology	24
3.1 Air Pollution on the Provincial Level	24
3.1.1 Calculating Aerosol Optical Depth	24
3.1.2 Estimating Ground Solar Radiation	26
3.1.3 Accuracy Assessment on the AOD Value	28
3.2 Land Surface Temperature on the City Level	28
3.2.1 Calculating Land Surface Temperature	28
3.2.2 Estimating Solar Panel Efficiency Based on Temperature	32
3.2.3 Selecting Solar-Efficient Areas Within City	34
3.3 Available Rooftop Areas on the Building Level	35
3.3.1 Processing LiDAR Data	35
3.3.2 Identifying Suitable Roofs	36
3.4 Energy Output Potential	40
Chapter 4. Results	41
4.1 Air Pollution	41
4.1.1 Annual AOD for Three Provinces.	41
4.1.2 Seasonal Aerosol Optical Depth within One City	43
4.2 Land Surface Temperature	44
4.2.1 Annual Land Surface Temperature for Three Cities	45
4.2.2 Monthly Land Surface Temperature within One City	47
4.2.3 Solar-Efficient Areas within One City	49
4.2.4 Final Selection of City Areas	50
4.3 Suitable Roofs	51
4.4 Daily Energy Output	53
Chapter 5. Discussions	54
5.1 Assessment of Results	54
5.1.1. Air Pollution	54
5.1.2 Land Surface Temperature	55

5.1.3 Suitable Roofs.....	58
5.2 Limitations	59
5.2.1 Limitations in Assessing Air Pollution	59
5.2.2. Limitations in Estimating Land Surface Temperature.....	59
5.2.3 Limitations in Identifying Suitable Roofs.....	61
5.2.4 Limitations in Calculating Daily Output.....	63
Chapter 6. Conclusions.....	65
References	67

Chapter 1. Introduction

1.1 Motivation

Affordable and clean energy (Goal 7) is one of the seventeen sustainable development goals (SDGs) announced by the United Nations in 2015. According to United Nations (2018), this goal is indicated by universal access to affordable energy and renewable energy share in total energy consumption by the year 2030; however, in the past years, progress in all areas towards this goal is impeded by inadequate policy commitment and the lack of willingness of countries to embrace new technologies.

Photovoltaic (PV) technology holds great potential to harvest the sun's energy as a source of electricity. For areas far from cities in developing countries, grid installation does not make economic sense to meet low energy demand with high infrastructure costs (Díaz, Arias, Peña, & Sandoval, 2010). Rooftop PV panels can provide such areas with affordable energy, and replace the traditional non-sustainable sources of energy such as wood (Akikur, Saidur, Ping, & Ullah, 2013). Rooftop PV system is a popular option for its cost-efficiency in land resources and transmission infrastructure. Even in countries with developed grid systems, PV technology is rising in popularity for renewable energy generation. It is the fastest growing renewable energy in Canada since 2004 (Natural Resources Canada, 2017), and among the mandatory targets for renewables in China (5 million KW by 2020) according to National Energy Administration (2016).

To foster greater commitment to this UN sustainable development goal, policy makers and urban planners may encounter practical issues to implement PV systems in local communities. As the environmental benefits do not pay for the cost of PV panel installation,

governments encourage renewable energy through subsidizing policies (Aguirre & Ibikunle, 2014). However, local PV energy production is dependent on climate (solar radiation), demand, socioeconomic factors (such as income and investment cost), and innovative and responsible behavior (Copiello & Grillenzoni, 2017). Decision-makers on the national level may be interested to know what regions they should direct public funding, while communities care more about the suitability of individual buildings for rooftop PV panels.

Thus, this project proposes a remote sensing framework to support decision making in rooftop PV development across different geographic scopes from cities to community rooftops. Specifically, for provincial administrations, this project compares the solar irradiance (also referred to as solar resource) which different cities receive after adjusting for the effects of air pollutions. For a city of strategic importance in solar resource, this project identifies the solar-efficient areas within its urban areas by considering the effects of urban heat island. For suitable buildings in the prioritized urban areas, this project calculates effective rooftop areas based on LiDAR-derived three-dimensional models and estimate the corresponding electricity output. This remote sensing project can empower decision makers to prioritize areas for PV development from cities to rooftops, for which they can provide policy and financial incentives accordingly to facilitate the progress towards the sustainable development goal.

1.2 Research Objectives

The research objective motivating this project is to support decision making in PV development from cities to community rooftops. To this end, the research question is how air pollution, land surface temperature, and building topographic factors influence the PV development in urban areas. Specifically, this project estimates the practical PV potential from

three levels including province, city, as well as building. To prioritize locations for PV installations, the project fulfills the following objectives:

1. On the provincial level, it quantifies the influence of air pollution on solar irradiance and identifies cities with abundant solar resources.
2. Within a significant city, it examines the spatial variation in land surface temperature and suggests thermal-efficient installation areas.
3. In a selected built environment, it determines the locations and areas of suitable roofs using LiDAR data.
4. It estimates daily power output based on ground-level solar radiation, solar cell efficiency, and available areas obtained from the steps above.

1.3 Study Area

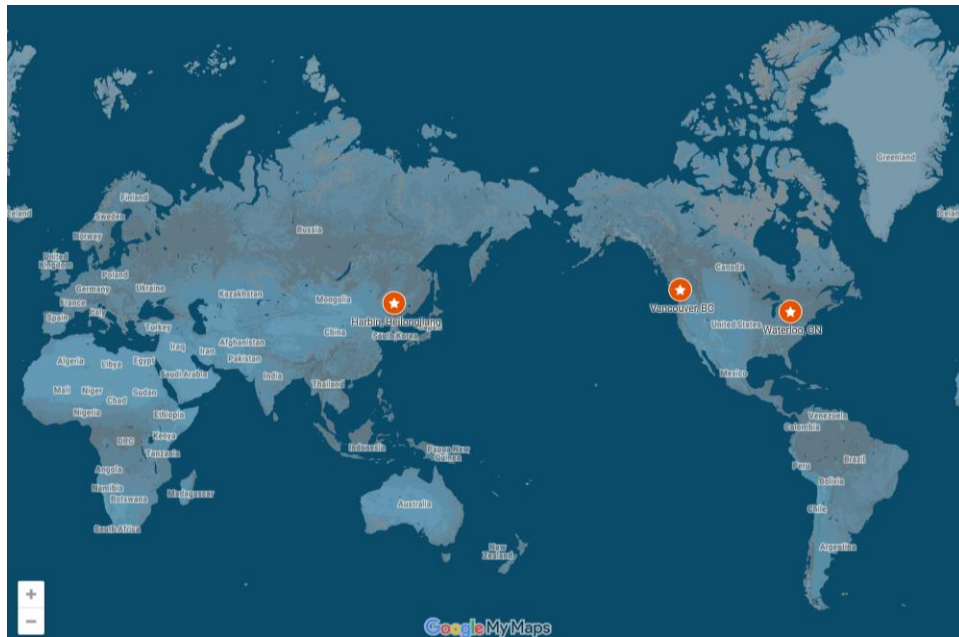


Figure 1-1: Cities of Interest, Google My Maps (2018)

This project focuses on three cities including Waterloo, Ontario and Vancouver, British Columbia in Canada, and Harbin, Heilongjiang in China. Referring to Figure 1-1, the three cities

are at similar latitudes in the Northern Hemisphere, and hence in similar positions to capture incoming solar radiation to the earth.

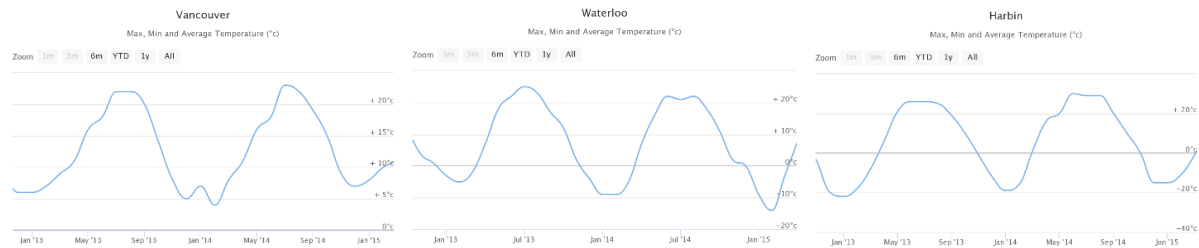


Figure 1-2: Average Air Temperature, World Weather Online (2018)

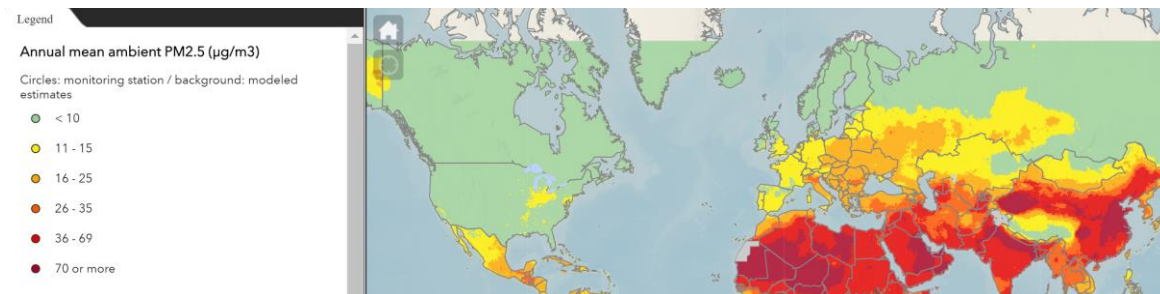


Figure 1-3: 2012-2016 Annual Average PM 2.5 Concentration, WHO (2016)

Air temperature and pollution data will be sampled from January 2013 to December 2014. Figure 1-2 demonstrates monthly air temperature. It is notable that the temperature in hot seasons is almost same in three cities, but in winter seasons Harbin is coldest, followed by Waterloo. Vancouver does not show temperature below zero. Figure 1-3 shows annual air quality indicated by the concentration ($\mu\text{g}/\text{m}^3$) of PM 2.5, which refers to particle matters with a diameter of 2.5 μm or less. Air quality is considered good when PM 2.5 level is lower than 12.0 $\mu\text{g}/\text{m}^3$, and unhealthy when it reaches 55.5 $\mu\text{g}/\text{m}^3$ or above (Mintz, 2009). World Health Organization [WHO] (2016) reported that Harbin is heavily polluted while Waterloo seems vulnerable to the air pollutant from the United States (Figure 1-3). Unlike ground-based measurement of air quality and air temperature, remotely sensed data allow people to understand how temperature and air pollution affect different parts of a city.

1.4 Roles of Project Members

In this project, Yunhong Tian led analysis related to air pollution; Zhihao Wang led analysis related to land surface temperature; Jiachen Wei led analysis related to three-dimensional roof modeling. Everyone in the project made contributions to the final reports, the poster, as well as the presentation. Additionally, Jiachen was responsible for connecting the objectives of this project to the UN sustainable development goals, Zhihao focused on data visualization, and Yunhong focused on reviewing writings.

1.5 Outlines

This report contains six chapters. Chapter 1 introduces the project motivation, research objectives, study areas, roles of project members, and finally, briefly outlines the report structure. Chapter 2 reviews previous literature on how air pollution, land surface temperature as well as regional geographic factors influence the rooftop photovoltaic development. At the end of this chapter, the research gap is discussed, and the rationale for this project is summarized according to previous literature. Chapter 3 describes the major methods used to prioritize locations for distributed generation from cities to regional rooftop. In addition, the process of data collection, data cleaning as well as data transformation are presented step by step. Chapter 4 analyzes the results and answers the research objectives defined in Chapter 1. All figures and tables for final visualization are demonstrated in this section. Chapter 5 further explains the results and confirms the validity by connecting them to previous studies. Additionally, the limitations existing in the datasets and methods are discussed by conducting the sensitivity analysis. Last, this chapter suggests the directions for future improvements. Chapter 6 summarizes the entire project regarding the project motivations, research objectives, and how these objectives are accomplished, as well as suggestions for future improvement.

Chapter 2. Background

2.1. Air Pollution

Aerosol optical Thickness (AOT) can quantitatively measure the loss of solar radiation due to aerosol scattering and absorption between the point of observation and the top of the atmosphere (Aloysius et al., 2008). AOT is another consideration to assess the suitability for photovoltaic development over a large geographic scale. The input data for analyzing air pollution is MOD04_L2 (Collection-6 Terra Product), which is level-2 MODIS atmospheric aerosol product with 10 * 10 km spatial resolutions offered by NASA. Based on the Dark Target (DT) and Deep Blue (DB) algorithms, the product covers aerosol properties across the entire globe. The output raster indicates AOT values (1000 times the actual values) in Lambert projection coordinate system. These product files are stored in Hierarchical Data Format (HDF-EOS) and contain the georeference information from the sensor, which can help with geometric correction. With a five-minute temporal resolution, MOD04_L2 allows for time series analysis to study the change in air quality and estimate future trends. These products can be accessed freely from NASA MODIS Adaptive Processing System, Goddard Space Flight Center. We intend to use monthly MOD04_L2 products from 2013 to 2017 to analyze the AOT value for our study areas. Using stratified sampling for every month, we will select one day at each air quality level (good, moderate, and unhealthy) to represent the average aerosol optical thickness. We intend to select the AOT product data at 12pm when the AOT value can represent the average value of the entire day (Mintz, 2009).

2.1.1 Dark Target Method

The basic method to obtain the AOD is called "Dark Target method " (DT), which is invented by Kaufman and Sendra (1988). The dense vegetation on the land, wet soil and water coverage has very low reflectance in visible wave band, which can be called dark pixels in remote sensing image. It is assumed that the DT's reflectance belongs to a constant ratio in short wavelength together with long wavelengths. Since aerosol has a proportionally greater effect on the shorter wavelengths, it is possible to invert a radiative transfer model to estimate the AOD that can provide the surface reflectances in the correct ratio(Holben, et.al, 2012). In the sky cloudless weather over the dark pixels, reflectivity observed from the satellite monotonously increases with the increase of aerosol optical thickness. The algorithm which uses this relationship to inverse atmospheric aerosol optical thickness, is known as the dark pixel method. Based on the atmospheric contribution of apparent reflectance, the DT method uses the spectral characteristics of low reflectivity of most land-surface in red (0.60-0.68 μm) and blue (0.40-0.48 μm) bands. According to (NDVI) or near-infrared channel (2.1 μm) reflectivity, the dark-pixels can be identified. Based on a certain relationship, DT method assumed the surface reflectance of these dark pixels in red or blue band, in order to invert the aerosol optical thickness. Initially, the method was applied only to areas where dense vegetation was known in advance. For better applicability of the method, Holben and Kaufman sought dark pixels in the mid-infrared band (2.1 μm or 3.8 μm). The surface reflectance relationship between the red reflectance (0.66 μm), the blue (0.47 μm) and the mid-infrared (2.1 μm) , which is obtained by fitting method. Then, they assumed the aerosol models which is suitable for their specific study areas. Next, the apparent reflectance obtained by the satellites can be used to invert the aerosol

optical thickness. Dark target method is currently the most widely-used algorithm retrieving aerosol optical thickness from remote sensing image (Gillingham; Flood; Gill; Mitchell, 2012).

However, there exist some limitations in the Dark Target method. To begin with, this method is based on the assumption of the use of an accurate radiative transfer model, which has been illustrated to be useful operationally by Ouaidrari and Vermote (1999). Nevertheless, the research was conducted in the specific study areas where the spectral reflectance of vegetation is almost close to zero, and the aerosol optical thickness value is fairly higher than usual values of my study. Furthermore, it is highlighted that Dark Target method is not suitable for the regions including Australia, Harbin and Canada, which is due to their drier climate and generally brighter vegetation (Kaufman and Sendra 1988). Moreover, the DT method was not based on actual measurements of vegetation's brightness, but historical vegetation maps which displays general classes. Also, the Dark-Target method has high bias when the study area is covered by urban area, owing to the surface assumptions. Unfortunately, the urban area will hold nearly three third of the world's census by 2025, despite it only makes up 0.5% on the surface of the earth (Pawan, Robert, Shana, 2014). The figure 2.1.1-1 shows the AOD Bias as function of percentage of Urban.

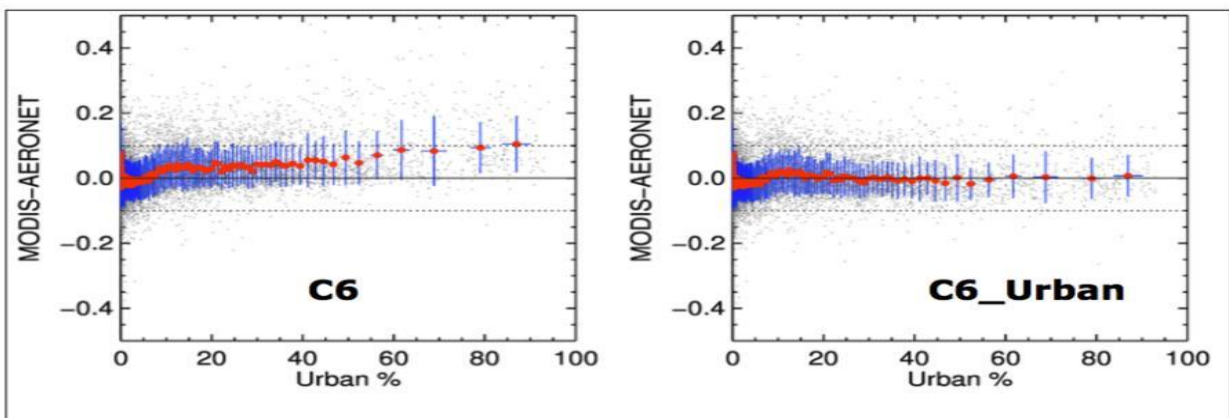


Figure 2.1.1-1 AOD Bias as function of percentage of Urban

2.1.2 Deep Blue Algorithm.

Since there is limitation of the design of the dark target algorithm: it is not for retrieving the aerosol optical thickness on desert and bright surfaces especially urban areas, in recent years, Hsu et al. (2004) have designed another algorithm to obtain the aerosol optical thickness over bright surfaces, which can make up significant gaps in world-wide aerosol sampling (e.g., Levy et al., 2007a and b). This algorithm can obtain the aerosol optical thickness through remote sensors over arid, semi arid, and urban areas are also taken into considerations. It was based on the principle that even the visually bright surface including desert can be with relatively low and stable surface reflectance in the deep blue wavelengths, especially 0.41 and 0.47 μm , so this algorithm is called Deep Blue (DB) (Sayer et al., 2013; Hsu et al., 2013). The main steps through the retrieval procedure are as followed:

2.2. Land Surface Temperature

Land surface temperature plays a crucial role in energy budget estimation, urban heat fluxes evaluation, as well as land cover and land use assessment (Chakraborty, Kant, & Mitra, 2015). The thermal infrared information from remote sensing imagery provides a valuable lens to explore and estimate land surface temperature (Caselles, Coll, Valor, & Rubio, 1997; Er-Raki, Chehbouni, Hoedjes, Ezzahar, Duchemin, & Jacob, 2008). This section reviews how previous methods measure land surface temperature, based on different remotely sensed imagery. Due to a lack of detailed research focusing on the study areas, this literature review searches all previous studies around the world to offer a comprehensive exploration of the solar energy group.

Currently, many algorithms have been investigated to estimate land surface temperature from remote sensing imagery (Liu & Zhang, 2011). There are four primary categories, including the Single Channel method (Price, 1983), the Split Window method (Wan & Dozier, 1996), the

Multi-Channel Temperature and Emissivity Separation method (Gillespie, Rokugawa, Matsunaga, Cothorn, Hook, & Kahle, 1998), Multi-Angle and Multi-Channel Combined method (Sobrino, Li, Stoll, & Becker, 1996). The rest part of this section mainly focuses on comparing and contrasting previous works which use two of these algorithms.

2.2.1 Single Channel Method

The Single Channel method employs an inversion of the radiative transfer model along with atmospheric profiles (e.g., water vapor) to compute the surface radiances and thus to estimate surface temperature (Kikon, Singh, Singh, & Vyas, 2016; Price, 1983; Scott & Chedin, 1981). To perform the model, the surface emissivity is required in advance. While the Single Channel method needs many parameters, the results are promised by these high-quality data. On the other hand, this algorithm is simple to employ if small errors can be tolerated in short-term projects.

Balçık (2014) collected meteorological data from 20 weather stations to validate the land surface temperature which was derived from the Single Channel method. In the study, the researcher also used Landsat 5 Thematic Mapper data in Istanbul, Turkey, in 2009 to perform the method. The results were improved by classifying land cover and land use first, and then estimating the land surface temperature individually, based on the classification results. The required land surface emissivity was calculated based on the Normalized Difference Vegetation Index using semi-empirical knowledge (Sun, Tan, & Xu, 2010; Zhang, Wang, & Li, 2006). The results demonstrated that there was a positive correlation between land surface temperature and the Index Based Built-up Index, which is proposed to measure a level of urbanization (Xu, 2007). Based on the correlation results, Istanbul was experiencing a detrimental development

with a decreasing area of natural vegetation. When validating the results from the Single Channel method, the study showed that the estimated mean temperature was 302.69 K, and the mean near-surface air temperature from meteorological stations was 301.83 K on September 5, 2009. This little difference (0.86 K) promised the accuracy of the Single Channel method. Besides, the correlation coefficient between the estimated surface temperature and the meteorological station derived temperature was 0.76, which indicated a strong relationship based on statistical confidence. In general, Balçık (2014) not only proved the results with ground truth data but also improved the accuracy of the Single Channel method with a pre-classification process. The merits of Balçık's work deserve to be used by the solar energy group to estimate land surface temperature.

Similarly, Coll et al. (2012) also used the Single Channel method to obtain land surface temperature but they evaluated their accuracy of different input remote sensing images. The objective of the study is to figure out which remote sensing data is most suitable for the Single Channel method. The researcher checked the accuracy from four satellite data, including Landsat 7-ETM+ band, Terra Advanced Spaceborne Thermal Emission and Reflection Radiometer (ASTER) bands 10-14, Terra Moderate Resolution Imaging Spectroradiometer (MODIS) bands 31 and 32, and Envisat Advanced Along Track Scanning Radiometer (AATSR) bands at 11 and 12 μm . The ground truth data was from the Valencia test site, and the atmospheric profiles were from Vaisala RS80 radiosonde balloons to compute local emissivity. The results demonstrated that ASTER data yielded the best overall accuracy with a small difference of 0.5-0.6K and biases within 0.2K. The followed satellite data was MODIS band 31 and 32, AATSR bands at 11 and 12 μm . The reason is that water vapor dominates in these windows, thus likely to introduce errors when performing the Single Channel method (Baldocchi, Falge, Gu, Olson, Hollinger,

Running, ... & Fuentes, 2001). Landsat had the worst agreement with the ground truth data but, in fact, the difference was acceptable, only about 1K. The merits of Coll's work were that they investigated the accuracy of the Single Channel method by comparing different input satellite data with a sensitivity and control test. Although the Landsat images had the lowest accuracy, the difference of 1K was still acceptable in a short-term project (Kikon et al., 2016; Liu & Zhang, 2011).

2.2.2 Split Window Method

The Split Window method, also called Two Channel method, is to utilize the difference of water vapor absorption between two adjacent infrared channels for retrieving land surface temperature (Becker, 1987; Coll & Caselles, 1997; Mao, Qin, Shi, & Gong, 2005). Semi-empirical parameters and the brightness temperatures in the two bands are used to estimate surface temperature. Unlike the Single Channel method, the Split Window method does not need the atmospheric profiles but requiring estimate the water vapor content, according to French et al. (2003).

A study from Begum et al. (2003) applied the Split Window method to estimate the surface temperature in the northwestern part of Bangladesh. In this work, twenty set of Pathfinder AVHRR Land (PAL) daily data were collected from March to October 1991 to perform the method. To compute the surface emissivity, the researchers used a same NDVI-based algorithm with Zhang et al. (2006) and Balçık's (2014) work. The novel improvement of this study was that they replaced the empirical parameters trained for a global scale with the parameters selected for the study area (tropical area). Their results indicated that there was a discrepancy in the estimated surface temperature between the parameters selected for tropical

areas and for worldwide. Among the measured surface temperature, the minimum and maximum discrepancy was 0.04 °C and 4.0 °C respectively; meanwhile, the average discrepancy ranges from 0.5 °C to 2.5 °C. However, this research failed to evaluate the accuracy of the Split Window method itself due to a lack of *in situ* data. The results of a comparison of the estimated surface temperature between different regions are dubious.

Comparatively, Labbi and Mokhnache (2015) obtained a convincing result of land surface temperature by using the Split Window method. In this work, the researchers selected two thermal infrared channels, IR 10.8 and IR 12.0, from the first Meteosat Second Generation satellite (MSG-1) data to perform the algorithm. The validation data were the *in situ* measured temperature from the African Monsoon Multidisciplinary Analysis. Their results were quite encouraging which were evaluated by sensitivity tests and a comparison with the validation data. The discrepancy between the estimated and the *in situ* temperature was 1.96K, and the root mean square error (RMSE) was 2.75K, both of which proved the accuracy of the Split Window method. From the sensitivity test, the authors indicated that the Split Window method was sensible to the possible errors from surface emissivity and atmospheric water vapor content. Although these errors limit all methods aiming to retrieve land surface temperature by using remote sensing images, the Split Window method reduces the errors by using the paired information from two adjacent infrared channels (Wan & Dozier, 1996; Yu, Guo, & Wu, 2014). The merits of this research proved that performing the Split Window method can produce accurate results without high-quality atmospheric data.

2.2.3 Limitations

Land surface temperature is one of the essential factors in solar energy estimation (Chakraborty et al., 2015). Its increasing importance leads to many proposed methods to accurately estimate land surface temperature. However, current methods are facing several challenges in this task: errors tend to be introduced by the complex atmospheric correction (Coll et al., 2007; Coll et al., 2012); uncertainties from thermal conditions have great impacts on temperature retrieval (Schmugge, French, Ritchie, Rango, & Pelgrum, 2002); acquiring high-quality satellite data with sufficient thermal infrared is quite difficult for most studies (Li et al., 2013; Sobrino & Jiménez-Muñoz, 2005); the complexity of separating temperature and emissivity limits current research (Coll et al., 2012; Zhang & Li, 2013); temporal changes of surfaces such as seasonal influence introduce the uncertainties of land classification (Balçık, 2014; Zhang et al., 2006). In addition to these common errors and uncertainties, two primary methods to estimate land surface temperature are discussed individually concerning their merits, limitations, feasibilities, errors, and uncertainties.

In general, the accuracy of the Single Channel method depends on the quality of the atmospheric profiles (Price, 1983; Scott & Chedin, 1981). As mentioned in Section 2.1, Coll et al. (2012) utilized the accurate atmospheric data to reduce the difference between the estimated and the ground truth temperature within 1K. However, the atmospheric data is difficult to acquire. To solve the high requirement, Zhang et al. (2006) proposed a NDVI-based method to replace the atmospheric profiles with surface radiances, which then be used to estimate land surface temperature. By sacrificing a bit of accuracy to reduce the high data requirement, this method has been widely used in a small project concerning urban heat island or urban energy estimations (Kikon et al., 2016; Liu & Zhang, 2011). Furthermore, Balçık (2014) improved the

accuracy of the NDVI-based method by classifying land cover and land use and then performing the Single Channel method. His results showed an encouraging accuracy: the difference between the estimated and the ground truth temperature was 0.86K. While the Single Channel method has a high requirement on the atmospheric profiles, the sacrifice of a bit of accuracy to simplify the model is acceptable in a short-term project (Sobrino, Jiménez-Muñoz, & Paolini, 2004).

However, limitations still exist in the Single Channel method: the uncertainties in surface emissivity are difficult to remove unless there are accurate atmospheric profiles (Coll et al., 2012). For a long-term remote sensing project, this proposed method is not qualified if there are no high-quality atmospheric profiles. In a short-term project or other applications of surface temperature (e.g., urban heat island), small errors may be tolerable. Thus, the Single Channel method is recommended to the solar energy group.

Comparatively, the Split Window method utilizes the paired information from two adjacent infrared channels to reduce the high requirement of atmospheric data (Yu et al., 2014). The study from Hulley et al. (2011) optimized the coefficients in the Split Window method to obtain more accurate results of global surface temperature in the water body. By performing a sensitivity test, the researchers indicated that potential errors introduced by sensor's viewing angle has relatively insignificant effects on the estimation of land surface temperature; the challenge of increasing accuracy still focus on the simulation of atmospheric data.

One of the most substantial uncertainties in the Split Window method is the information of band emissivity, which is indirectly acquired from two adjacent infrared bands (Zhang & Li, 2013). To some extent, if the coefficients in the Split Window method are optimized by considering local atmospheric situations, its results can outperform the Single Channel method in

terms of the complexity of model performance and the accuracy of temperature estimation (Hulley et al, 2011). According to Yu et al. (2014), the Split Window method has a smaller RMSE (1.025K) than the Single Channel method (1.39K) when they used same remote sensing data to compare the accuracy of these two methods. Therefore, previous works have proved that the Split Window method has low data requirement and can produce a more accurate estimation of land surface temperature. Based on these merits, the Split Window method is recommended to the solar energy group.

2.3. Topographic Factors for Rooftop Photovoltaic Installation

The project considers the slope (altimetry), aspect and area (planimetry), and the shading (obstructions) of the surrounding terrain, vegetation, and built environment. Surface availability of building roofs is examined for the calculation of effective rooftop area.

Light Detection And Ranging (LiDAR) point clouds can help identify such characteristics. Three dimensional (3D) coordinates of the points on a surface can represent the surface at sufficient sampling density. LiDAR is a surveying method to obtain the 3D location (x,y,z) of a target from a ground-scanning airborne laser. Digital surface model (DSM) indicate the elevation of topographic features on the bare earth at a given spatial resolution (raster cell size), and it can be derived from LiDAR data.

The City of Vancouver LiDAR (2013) is open to the public. The LiDAR data was collected on February 7, 15 and 19, 2013, and stored as one square kilometer tiles in LAS and GeoTIFF formats. There are at least 12 points in one square meter, with a horizontal accuracy of 0.36 m and a vertical accuracy of 0.18 m (95% confidence level). The data is available to public from City of Vancouver's Data Catalog. Both formats are georeferenced to UTM Zone N10, with NAD 83 as the horizontal datum and CGVD28 as the vertical datum.

2.3.1 Area

Few studies considered roof area when assessing the roof suitability. Chow, Li, & Fung (2016) applied a packing factor of 47.5% to account for the maintenance requirement that solar panels cannot cover the entire roof. Boz, Calvert & Brownson (2015) obtained roof segments as the result of intersecting the classified slope polygons (7 classes from 0° to 90°) with the classified aspect polygons (5 classes including horizontal, north, east, south, and west). Referring to Figure 7, it can be difficult in this approach to select priority rooftop areas based on the segments because many segments (red lines) within the building footprint (blue line) are too small for PV installation.

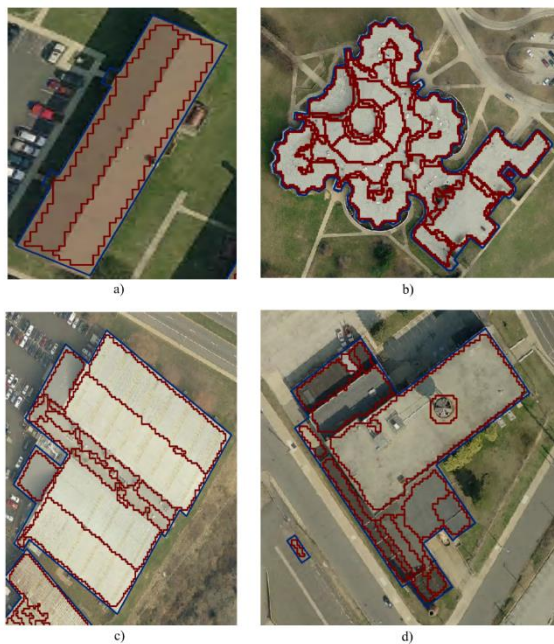


Figure 2.3-1: Rooftop Segments (Boz et al.,

In Figure 2.3-1, while simple rooftop (Figure 2.3-1a) was precisely segmented into two polygons, the complex rooftops were overly segmented due to roof ridges (Figure 2.3-1b) and false slope identification (Figure 2.3-1c). Small rooftop structures were overlooked (Figure 2.3-

1d) due to insufficient LiDAR point density. Overall, this approach should be avoided in our project. Instead of intersecting two layers of polygons, aspect information can be calculated for each slope polygon.

2.3.2 Shading

Shading of terrain, vegetation, and surrounding buildings is a dynamic cause of irradiation loss. Even though the topographic surroundings remain the same, the length of a shadow changes for different times of the year.

Adjustments specific to latitude and longitude were devised. Chow et al. (2016) applied a global shading factor of 65% for Toronto. Boz et al. (2015) applied a shading constraint in Philadelphia, eliminating shaded locations between 9 am to 3 pm at the summer solstice and between 10 am to 2 pm at the winter solstice. Our project can explore the potential of elevation data to address the shading factor.

2.3.3 Aspect

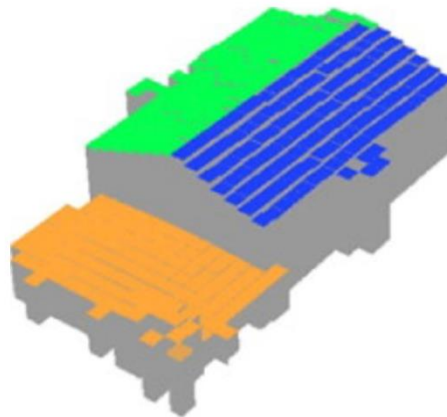


*Figure 2.3-2: Aspect Segmentation
(Lukač, Žlaus, Seme, Žalik, & Štumberger, 2013)*

Aspect (also known as azimuth) refers to the direction that a sloping surface faces. It is

measured in degrees, with values increasing clockwise from the North (0°) to the maximum 360° . The aspect of a horizontal (slope = 0°) roof will be marked as -1 (aspect neutral) in our project. Aspect values can be generated from DEM data for both raster and vector surfaces in ArcGIS (Figure 2.3-2).

In the northern hemisphere, the south orientation (aspect = 180°) allows for maximum PV energy output, which decreases as the roof surface turns eastwards or westwards (Lahnaoui et al., 2017). Referring to Figure 2.3-3, a south-facing or horizontal roof (aspect = 180° or -1) will be considered the optimal orientation in the project, while north-oriented sloping roofs (aspect close to 0° or 360°) being the least efficient for energy yield. The relationship is “conceptual” because it may not be linear for sloping roofs.

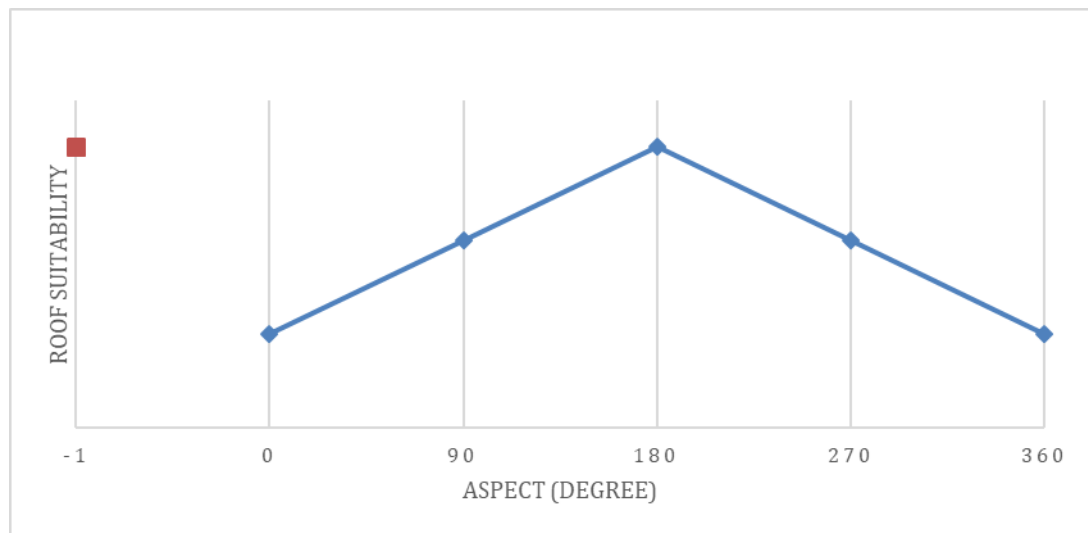


Figure 2.3-3 Conceptual Relationship between Aspect and Roof Suitability

2.3.4 Slope

Slope of a roof surface is also referred to as tilt or steepness. It is a value from 0 degree to 90 degrees, with 0 indicating a horizontal surface parallel to the surface of the reference ellipsoid. Although many studies used a single threshold for roof slope (such as 15 degrees or 30 degrees), more accurate results were produced by less aggregated classification (Alexander, Smith-Voysey, & Tansey, 2009). According to Zhou, Zheng, & Grigoropoulos (2012), the optimal tilt angle for energy yield varies for different latitudes by studying three cities from N30° to N45° in the United States.

The desirable tilt angle for solar panels is not a constant value. To expose the solar panel to maximum amount of radiation, Statler, Adams, & Eckmann (2017) suggested greater tilt angle in winter while smaller in the summer according to changes in solar declination. Lahnaoui et al. (2017) identified a range of optimal title angles from 30° to 45° for roof surfaces in different orientations. In practice, an approximate 30° angle off the horizontal is recommended for rooftop solar panels by the Green Age (2018) for the fixed solar panel to most efficiently receive solar irradiance. Energy Sage (2018) suggests that a tile angle close to 30° increases energy yield, and a sloping roof at this angle reduces the costs for installation. Roof slope over 60° is disregarded for PV panel installation (Boz et al., 2015; Jakubiec & Reinhart, 2013).

Roof slope can be calculated from LiDAR data in ArcGIS. It is equated to the maximum change in elevation values in a cell. To eliminate errors in the LiDAR data caused by unexpected objects between the laser and the roof surface, Majority Filter can be applied to correct the erroneous cell values based on the neighboring cells. To integrate the following factors into our analysis, the identified rooftop surfaces will be converted from raster to vector polygons with a slope attribute.

2.3.5 Rooftop Structures

Effective rooftop area accounts for installation density and areas occupied by structures such as chimneys and HVACs. Previous studies used the following methods to determine the available rooftop area.

2.3.5.1 Global Corrective Factor

This approach calculates effective rooftop area through multiplying the gross rooftop area by one or more global corrective factors. Paidipati, Frantzis, Sawyer, & Kurrasch (2008) and Chow et al. (2016) identified six corrective factors. Among these factors, slope, orientation, and shading are considered by our project; aesthetic appeal is relevant but not considered by the literature; structural soundness is considered adequate to support the load of solar panels because of the building code requirements. After all, the only functioning corrective factor is the module coverage factor (the packing factor), which accounts for the maintenance requirement for solar panel density. Empirical studies applied a module coverage factor of 50% in Texas (Paidipati et al., 2008) and 45% in Italy (Bergamasco & Asinari, 2011).

2.2.5.2 Digitization

Compared to applying an overall corrective factor, this approach is more accurate for individual rooftops. Using high-resolution orthoimage in GIS software, this approach deducts the rooftop areas occupied by structures such as chimneys and HVACs. For our project, manual digitization is feasible when a limited number of buildings are prioritized within a city.

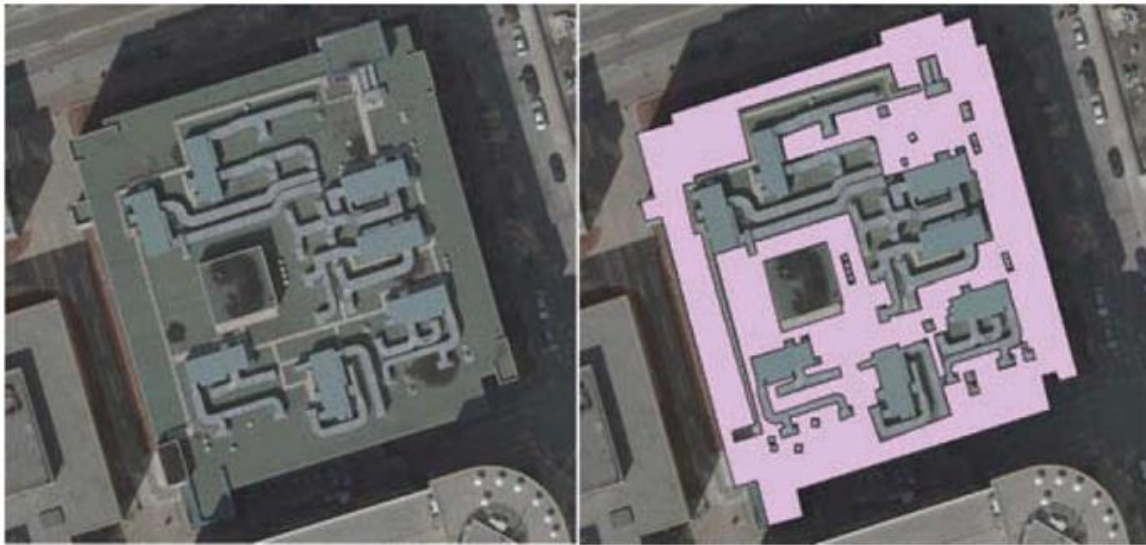


Figure 2.3-4: Example of an Overly Occupied Rooftop (Chow et al., 2016)

Shading factor and packing factor are applicable to the digitized area. For example, a packing factor of 0% can be used to disregard a roof that is intensively segmented by rooftop structures (Figure 2.3-4). Corrective factors used in the digitization approach can be specific to the geometry of individual roofs.

2.2.5.3 LiDAR

LiDAR is considered the optimal approach to measure detailed roof structures and urban landscape (Jakubiec & Reinhart, 2013). Referring to Figure 2.3-5, the LiDAR point data are first categorized into building and ground (including vegetation), and then triangulated into a surface model.

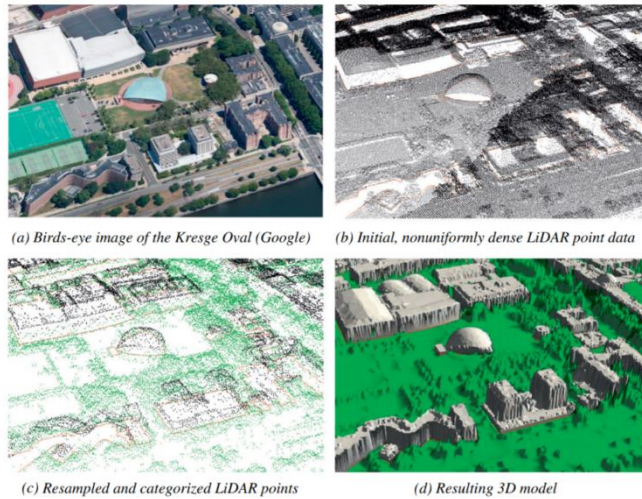


Figure 2.3-5: LiDAR 3D Modelling (Jakubiec & Reinhart, 2013)

While LiDAR data holds the potential to identify rooftop structures based on elevation difference, previous studies merely extracted building footprints from LiDAR points (Lukač et al., 2013; Kodysh, Omitaomu, Bhaduri, & Neish, 2013; Huang et al., 2015). Our project extracts from high density LiDAR data the suitable rooftop area instead of using the gross rooftop area.

Chapter 3. Methodology

3.1 Air Pollution on the Provincial Level

This section describes the methods used to select the most suitable province with the least air pollution, which may have the least loss of solar radiance owing to the air pollution. Aerosol optical Depth (AOD) can quantitatively measure the loss of solar radiation due to aerosol scattering and absorption between the point of observation and the top of the atmosphere (Aloysius et al., 2008). Therefore, it is another consideration to assess the suitability for photovoltaic development over a large geographic scale. Specifically, Section 3.1.1 describes the pre-processing and processing procedure on the MODIS aerosol product to retrieve the AOD value. Section 3.1.2 introduces the Bird Model Software and its theory to calculate the solar radiance and its loss owing to the air pollution. Last, section 3.1.3 will display the accuracy assessment method on the AOD value.

3.1.1 Calculating Aerosol Optical Depth

The MODIS Conversion Toolkit (MCTK) is used to import the MODIS aerosol product and pre-process the data, which is a plugin module for ENVI to convert the MODIS product from HDF4 format to other general format that can be imported into ArcGIS (Yale University, 2018). After pre-processing the data by MCTK, it is important to extract the data by the province boundary mask. The extracted raster data will be mosaic into new raster. Using the "raster statistics" in ENVI, the average pixel value is the mean value of AOD of the province. The workflow of calculating AOD value is displayed in figure 3.1-1.

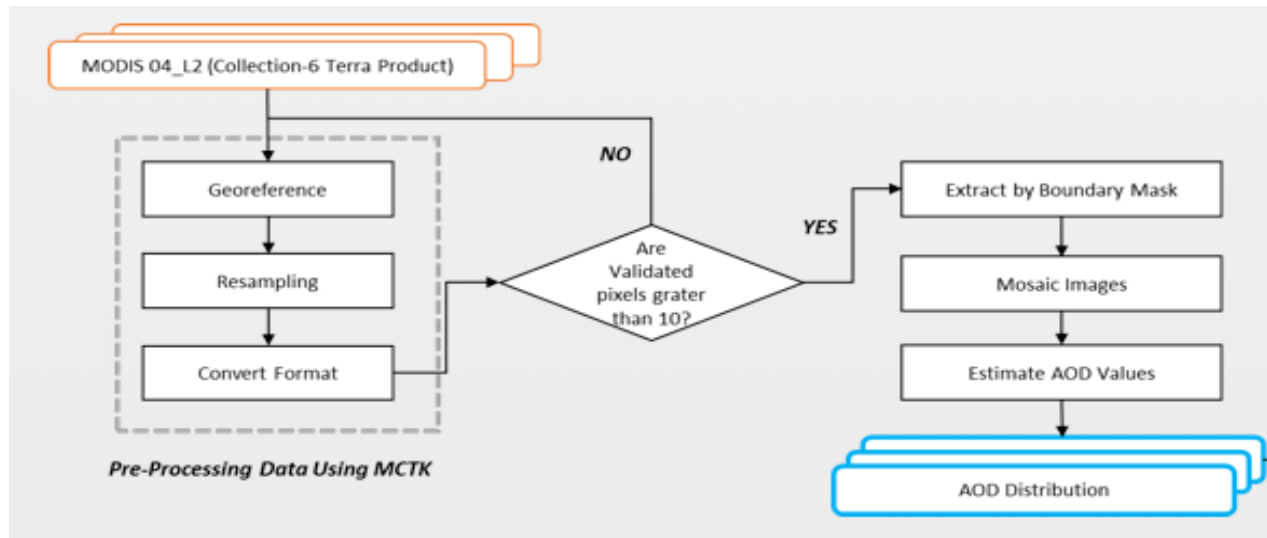


Figure 3.1-1 the workflow of calculating aerosol optical depth

The input data used for retrieving AOT value is MOD04_L2 (Collection-6 Terra Product), which is level-2 MODIS atmospheric aerosol product offered by NASA. There are two categories of product with two different spatial resolutions: one is 3 km* 3 km, the other is 10 km * 10 km. Considering the scale of the study area and the requirement of accuracy, the data for analysis is in 3km *3km spatial resolution. Based on the Dark Target (DT) and Deep Blue (DB) algorithms, this product can cover aerosol properties across the entire globe. The projection coordinate system of output raster indicating AOT values (equal to the actual values) is Lambert. The MODIS_04 files are stored in Hierarchical Data Format (HDF-EOS). In addition there exists georeference information from the sensor in the folder, which can be helpful to geometric correction. It is noticeable that this product is in a five-minute temporal resolution, thus analysing time series suitably and studying the variation in air quality and estimating future tendency. These products can be accessed freely from NASA MODIS Adaptive Processing System, Goddard Space Flight Center. We intend to use monthly MOD04_L2 products from 2013 to 2017 to analyze the AOT value for our study areas. Using stratified sampling for every

month, we will select one day at each air quality level (good, moderate, and unhealthy) to represent the average aerosol optical thickness. We intend to select the AOT product data at 12pm when the AOT value can represent the average value of the entire day (Mintz, 2009).

To begin with, the data is georeferenced by MCTK, using their georeference file from the sensor with longitude and latitude information. The new projected systems selected for British Columbia, Ontario, and Harbin is UTM_NAD_1983, UTM_NAD_1983, WGS_1984 respectively. In addition, the data is resampled and converted to dat format, which can be input and processed easily by ENVI and ArcGIS.

After pre-processing the data, it is of significance to import the pre-processed data to ArcGIS and check whether there are more than 10 validated pixels within the study area. If the number of validated pixels in the study area is less than 10, the data will be removed from the contents. After the judgement on the number of pixel, the suitable data will be mosaic to new raster. Then the province boundary shapefiles will be used as masks to extract the new raster within the province boundary. The output raster data are the final AOD data which will be used to analyse the AOT distribution and compare the different air pollution situation in three study areas. Last, the final AOD data will be import in ENVI. Using "Raster Statistics", the minimum, maximum and average pixel value can be summarized, which can reflect the different AOD situation and air quality of three study areas.

3.1.2 Estimating Ground Solar Radiation

The Bird Clear Sky Model is the software used to estimate the solar radiance of clear sky direct beam on the horizontal surface, authored by Richard Bird. The theory of this model was introduced in section 2.1.2. Since this model is based on empirical representations of radiative

transfer equations and attempts to take into account the cumulative effects of aerosols, water vapor, ozone and other gases, and Rayleigh (molecular) scattering upon sunlight reaching Earth's surface. It is of significance to acquire the longitude, latitude, elevation, exact date and time, sea level, total column ozone, total precipitable water vapor and AOD value at the same time. The climate and atmosphere data can be acquire from Atmosphere Science Data Center by NASA, which is the enhanced GIS-enabled data service page. The interface of the Bird Clear Model is shown in figure 3.1.3. The percentage of loss for each type of solar radiation and for total radiation at different AOT will be calculated according to the Equation 3-1.

$$\text{solar radiation loss (\%)} = \left[1 - \frac{\text{lowest value of solar radiation}}{\text{highest value of solar radiation}} \right] \quad (3-1)$$

Inputs:

Quantity	Units	Value
Mean (1 AU) solar constant	W/m ²	1367
Longitude	degrees (West is "-")	-75
Latitude	degrees (North is "+")	40
Elevation	meters	120
Month	1-12	6
Day	1-31	21
Year	20xx	2007
Hour	1-24 UT	17
Minute	1-59	0
Second	1-59	0
Sealevel ("weather report") pressure	millibars	1012
Surface albedo	(dimensionless)	0.2
Total column ozone	atm-cm	0.3
Total precipitable water vapor	cm H ₂ O	1.5
Aerosol optical depth @ 500 nm	(dimensionless)	0.10
Aerosol optical depth @ 380 nm	(dimensionless)	0.15

Click to calculate outputs...

Click to reset values to defaults...

Outputs:

Quantity	Units	Value
Julian Date	Days	
Station pressure	mbar	
Earth/sun distance	AU	
Solar zenith angle	degrees	
Relative air mass	(dimensionless)	
Distance-corrected solar constant	W/m ²	
Direct irradiance on horizontal surface	W/m ²	
Diffuse irradiance	W/m ²	
Total irradiance on horizontal surface	W/m ²	

Figure 3.1.3 the screenshot of the Bird Clear Model

3.1.3 Accuracy Assessment on the AOD Value

Accuracy will be assessed using ground-based measurement. The validation data is the surface AOT data from spectrophotometer provided by AERONET's aerosol measurement networks. Based on the space-time matching methods, the accuracy of AOT value from MODIS product can be assessed through the following steps. (1) Select 5×5 grids (10 km * 10 km per grid) which use AERONET observation sites in Waterloo, Vancouver and Harbin as the center. (2) Select the corresponding ground data observed from AERONET within 30 minutes before and after the satellite transit, during which there are usually 4 or 5 observations. Specific statistics also requires that MODIS data have at least 5 grid points in every 25 grids, equivalent to an area of 50 km * 50 km. The space-time matching will fail if there are fewer than two observations within 30 minutes before and after the satellite transit. (3) After comparing the surface value of AOD and the average value from MODIS product, the accuracy of the AOT product will be produced.

3.2 Land Surface Temperature on the City Level

This section describes the methods used to select one of the most solar-efficient cities. Specifically, Section 3.2.1 introduces the Single Window method employed to retrieving land surface temperature. Section 3.2.2 shows the linear regression used to quantitatively measure the relationship between land surface temperature and solar panel efficiency. Last, Section 3.2.3 demonstrates the process of how to select the most solar-efficient areas within one city.

3.2.1 Calculating Land Surface Temperature

The Single Window method was used in this project to calculate land surface temperature. As mentioned in the background section, the Single Window method employs an

inversion of the radiative transfer model along with atmospheric profiles (e.g., water vapor) to compute the surface radiances and thus to estimate surface temperature (Kikon et al., 2016; Price, 1983). To perform the model, the surface emissivity is required in advance. While the Single Channel method needs many parameters, the results are promised by these high-quality data (Scott & Chedin, 1981). Moreover, this algorithm is simple to employ in a short-term project. The main workflow in calculating land surface temperature is shown in Figure 3.2-1.

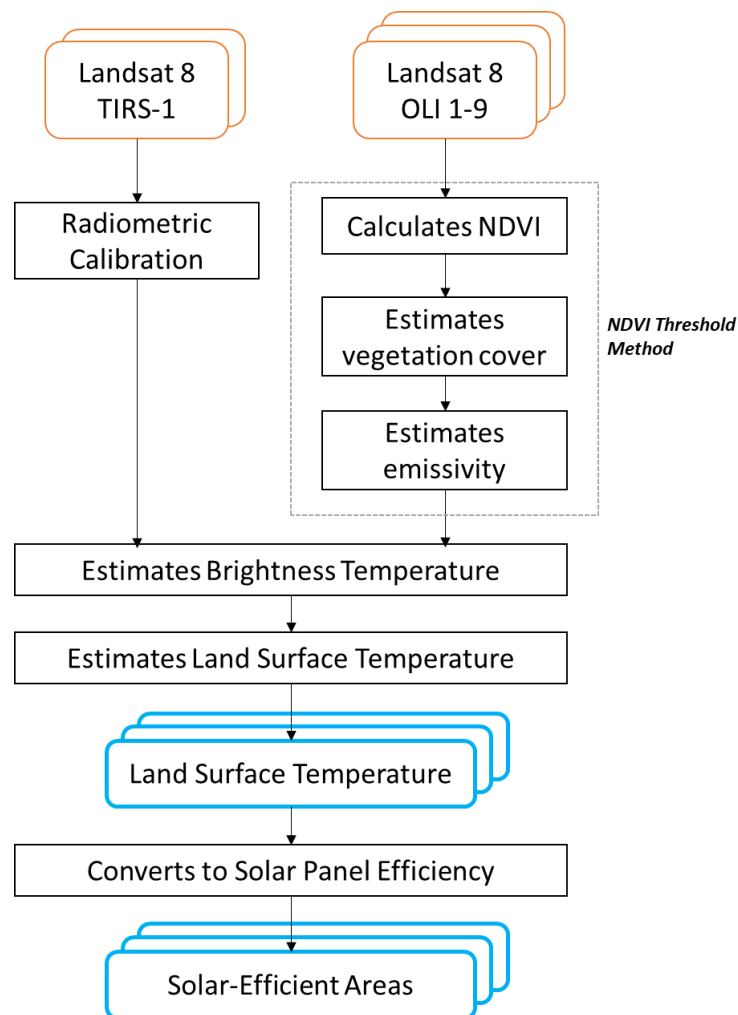


Figure 3.2-1. Workflow Chart of the Single Window Algorithm

The input data is Landsat 8 Thermal Infrared Sensor (TIRS) Band 10 and Operational Land Imager (OLI) Sensor Band 1-9. Landsat 8 data used in this project were downloaded from the Earth Explore, which is supported by the U.S. Geological Survey and offers free satellite images for scientific research (USGS, 2018).

The first step is to convert spectral radiance of TIRS-1 into Atmospheric Spectral Radiance. According to Jiménez-Muñoz et al. (2014), TIRS-1 (Band 10) is more accurate than TIRS-2 (Band 11) to retrieve land surface temperature because TIRS-1 is installed in a lower atmospheric absorption region. Thus, this project only used the TIRS-1 as the input thermal data. The Radiometric Calibration in ENVI was used to implement this step.

Second, land surface emissivity is estimated by using the NDVI Thresholds method from Sobrino et al. (2008). Normalized Difference Vegetation Index (NDVI) is a widely used index to quantify vegetation in remote sensing data. NDVI can be calculated by using Equation 3.2-1 but this project used the NDVI tool in ENVI directly. Next, Fractional Vegetation Cover (FVC) is estimated from NDVI data by using Equation 3.2-2. FVC refers to the proportion of vegetation in land surface. To perform this equation, this project used empirical parameters to extract the soil pixels ($NDVI \leq 0.05$) and pixels of full vegetation ($NDVI \geq 0.7$) (Sobrino et al., 2008). Last, land surface emissivity (LSE) was estimated from the FVC data by using Equation 3.2-3. LSE is a substantial factor to measure transmitting thermal energy from surface to atmosphere (Valor & Caselles, 1996). Based the research from Sobrino et al. (2008), the empirical emissivity was 0.986 for soil and 0.99 for vegetation. All the equations used in the NDVI Threshold method were implement using Band Math tool in ENVI.

$$NDVI = \frac{NIR-Red}{NIR+Red} \quad \text{equation 3.2-1}$$

where:

NIR = OLI Band 5

Red = OLI Band 4

$$FVC = \left(\frac{NDVI - NDVI_{Soil}}{NDVI_{Vegetation} - NDVI_{Soil}} \right)^2 \quad \text{equation 3.2-2}$$

where:

$NDVI_{Soil} = NDVI$ if $NDVI \leq 0.05$

$NDVI_{Vegetation} = NDVI$ if $NDVI \geq 0.7$

$$LSE = \varepsilon_s \times (1 - FVC) + \varepsilon_v \times FVC \quad \text{equation 3.2-2}$$

where:

FVC = fractional vegetation cover

$\varepsilon_s = 0.971$, emissivity for soil in TIRS-1

$\varepsilon_v = 0.987$, emissivity for vegetation in TIRS-1

(Sobrino et al., 2008)

Third, brightness temperature is estimated by using the calibrated TIRS-1 (step 1) and land surface emissivity (step 2). Different from traditional methods, this project reduced the atmospheric interaction by using a radiative transfer model. According to Tardy et al. (2016), the radiative transfer model can reduce the atmospheric effects on the conversion from sensor radiation to surface radiance. The mathematical expression of this model is shown in Equation 3.2-4, which requires the vertical atmospheric data including the atmospheric transmittance, the upwelling atmospheric radiance and the downwelling atmospheric radiance. All these atmospheric data were collected for each image from NASA atmosphere website (Atmospheric Correction Parameter Calculator, 2018).

$$\text{Brightness Temperature} = \frac{SR - L_u - \tau \times (1 - LSE) \times L_d}{LSE \times \tau} \quad \text{equation 3.2-4}$$

where:

SR = spectral at-sensor radiance

LSE = land surface emissivity

τ = the atmospheric transmittance

L_u = the upwelling atmospheric radiance

L_d = the downwelling atmospheric radiance

(Tardy et al., 2016)

Last, land surface temperature is converted from the derived brightness temperature. The basic Planck's Law was used to perform the data conversion, and a simplified Planck's radiance function is shown in Equation 3.2-5. More importantly, this equation requires the pre-launch calibration constants including K_1 and K_2 , which can be found in the metadata and are consistent with all images in Landsat 8 Band 10.

$$\text{Land Surface Temperature} = \frac{K_2}{\ln(1 + \frac{K_1}{BT})} \quad \text{equation 3.2-5}$$

where:

BT = brightness temperature

$K_1 = 774.89$, the pre-launched calibration constant 1

$K_2 = 1321.08$, the pre-launched calibration constant 2

(Tardy et al., 2016)

3.2.2 Estimating Solar Panel Efficiency Based on Temperature

A linear relationship is described in this section to estimate solar panel efficiency based on different land surface temperature. According to Dubey et al. (2013), the operating temperature of solar panels plays a crucial role in the process of the photovoltaic conversion. Based on empirical experience, as the temperature of solar panels increases, their voltage output will decrease linearly. Thus, this project measures the effect of land surface temperature on solar panel net efficiency using the linear parameters from the Dubey's work: the slope is -0.0615 while the intercept is 16.5375 (Figure 3.2-2). The Band Math in ENVI was used to perform this conversion.

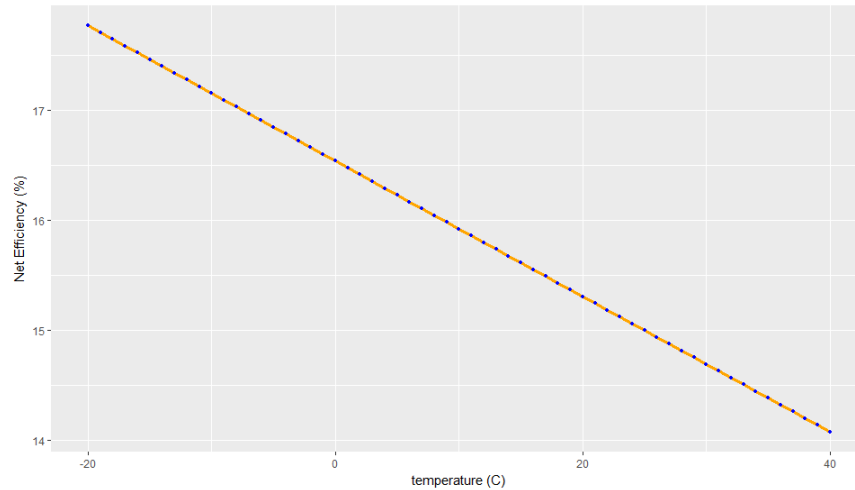


Figure 3.2-2 Linear Relationship Between Temperature and Solar Panel Net Efficiency

There is one limitation existing in this method. The used linear parameters were estimated for a global level in the research from Dubey et al. (2013). While they are more general and suitable for the three cities in this project, more accurate parameters are expected for a city level. Additionally, different solar panels have different abilities to convert photovoltaic energy. This difference may introduce the bias to this project which aims to estimating distributed generation for local governments. In the discussion part, this limitation is explored in detail.

3.2.3 Selecting Solar-Efficient Areas Within City

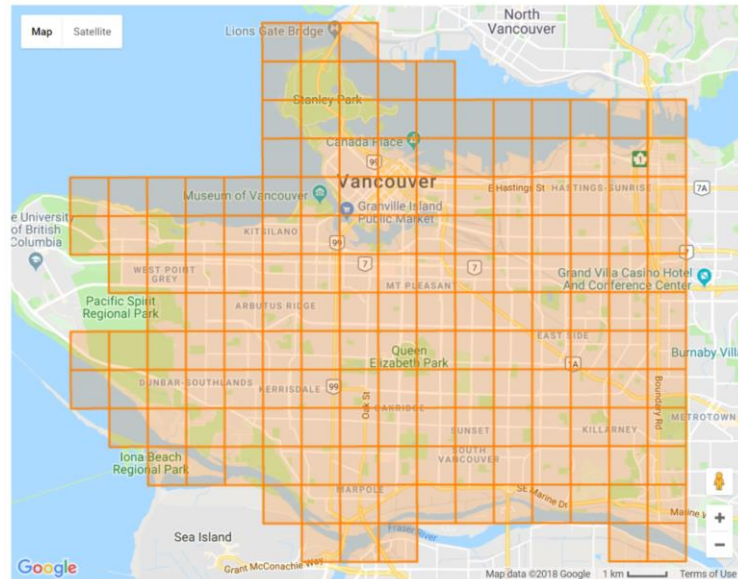


Figure 3.2-3 Data Tiles of the City of Vancouver LiDAR (2013)

The solar-efficient areas within one city are selected by considering the urban heat island. The urban heat island refers to the metropolitan area that is typically warmer than suburban area due to human activities (Stone & Rodgers, 2001). This project takes into account the regional distribution of solar-efficient areas. In order to help 3D modeling process, the tiles storing LiDAR data are regarded as the basic research unit to measure urban heat island effects. Take the City of Vancouver as an example, their LiDAR data is stored in grid cells around the city (Figure 3.2-3). Thus, the average land surface temperature is calculated for each tile. The Zonal Statistics tool in ArcGIS was used to perform this aggregation process.

3.3 Available Rooftop Areas on the Building Level

This section explains how suitable roofs were identified as polygons from LiDAR data. The steps are outlined in Figure 3.3-1. Section 3.3.1 describes how building roofs were extracted from LiDAR cloud points in ENVI LiDAR, and Section 3.3.2 lists the steps to assess the roof polygons PV system suitability in ArcMap.

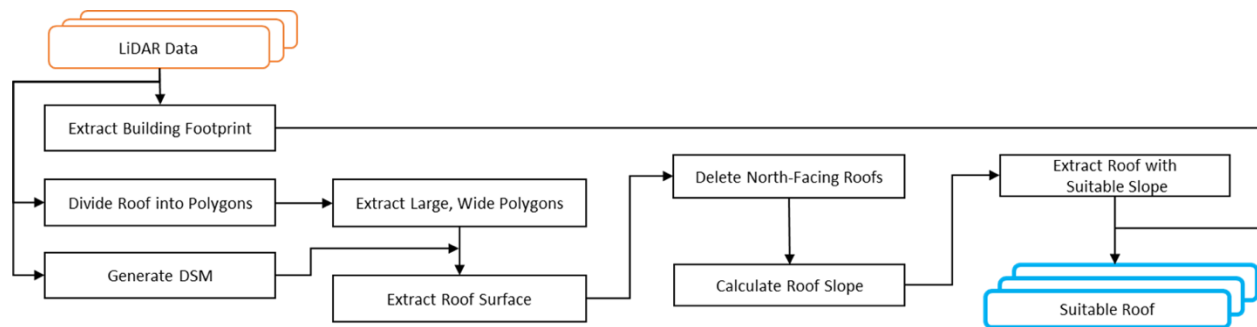


Figure 3.3-1 Steps to Identify Suitable Roofs

3.3.1 Processing LiDAR Data

ENVI LiDAR 5.4 is able to extract DSM, buildings, trees, etc. from LiDAR raw data (Harris Geospatial Solutions, 2018). The City of Vancouver LiDAR (2013) data was collected on February 7, 15 and 19, 2013, and stored as one square kilometer tiles in LAS and GeoTIFF formats. The project assessed the building in three 1 km² areas with the most suitable land surface temperature for solar panels.

First, each 1 km² LiDAR data tile (in las format) was imported to ENVI LiDAR and referenced to UTM Zone N10 in the NAD 83 datum. A density map was generated to examine the density and coverage of the data points, and they matched the reported figures (about 12

points per square meter and full coverage in each 1 km² tile). This is very good point density to represent a detailed 3D city.

Second, the Process Data tool was used. Buildings and DSM were selected as the output. The Buildings algorithm searches all flat surfaces and creates a roof polygon representing each of them. The area of a roof polygon was specified as the default 10 m² because they would be further classified into available areas and rooftop structures (such as chimneys). Others parameters were also kept at default values including the width of near-ground objects and vertical tolerance for neighboring points. Two shape files were created for each LiDAR data tile: building foot print and multiple roof polygons within each building footprint. The DSM resolution was specified as 1 meter and the output raster was in dat format.

To ensure the quality of the vector outputs, the roof polygons were manually corrected in the AQ Mode. A very small number of large building that had not been identified were manually constructed, and large vehicles were deleted. The reprocessed vector data were exported.

3.3.2 Identifying Suitable Roofs

The output roof polygons, building footprint, and DSM raster were loaded into ArcMap 10.5.1. The output of this section is the roof polygons that are suitable for PV panel installation with their areas calculated.

First, large and wide roof polygons were extracted from all the roof polygons. These polygons were identified as separate from the others because of different elevation values. Roof polygons of small sizes are difficult for solar panel installation and maintenance, and some of

them are covered by tree canopies or rooftop structures such as heating and ventilation facilities. The roof polygons were classified by shape area in quantiles (24.00 m² for Tile 25, 29.87 m² for Tile 32, and 44.60 m² for Tile 44), and the lower quantiles were deleted as appropriate for individual areas. Figure 3.3-2 shows an example of the classification results of the roof polygons in a selected tile, from which the polygons smaller than 24 m² were removed.



Figure 3.3-2 Roof Polygons Classified by Area

From the remaining roof polygons, narrow roofs (shape area/shape length < 1m) were removed. This is because common solar panels are approximately 1m wide. Figure 3.3-3 highlights the narrow roofs in the same area.



Figure 3.3-3 Example of Narrow Roofs

Second, the aspect of the remaining roofs was considered. The DSM raster was clipped to within the large and wide roof polygons. The Aspect tool identified the aspect of each raster cell based on the maximum rate of change from its neighbors. Referring to Figure 8, the aspect values range from 0 degree (North) clockwise to 360 degrees, with an additional value of -1 indicating flat roof.

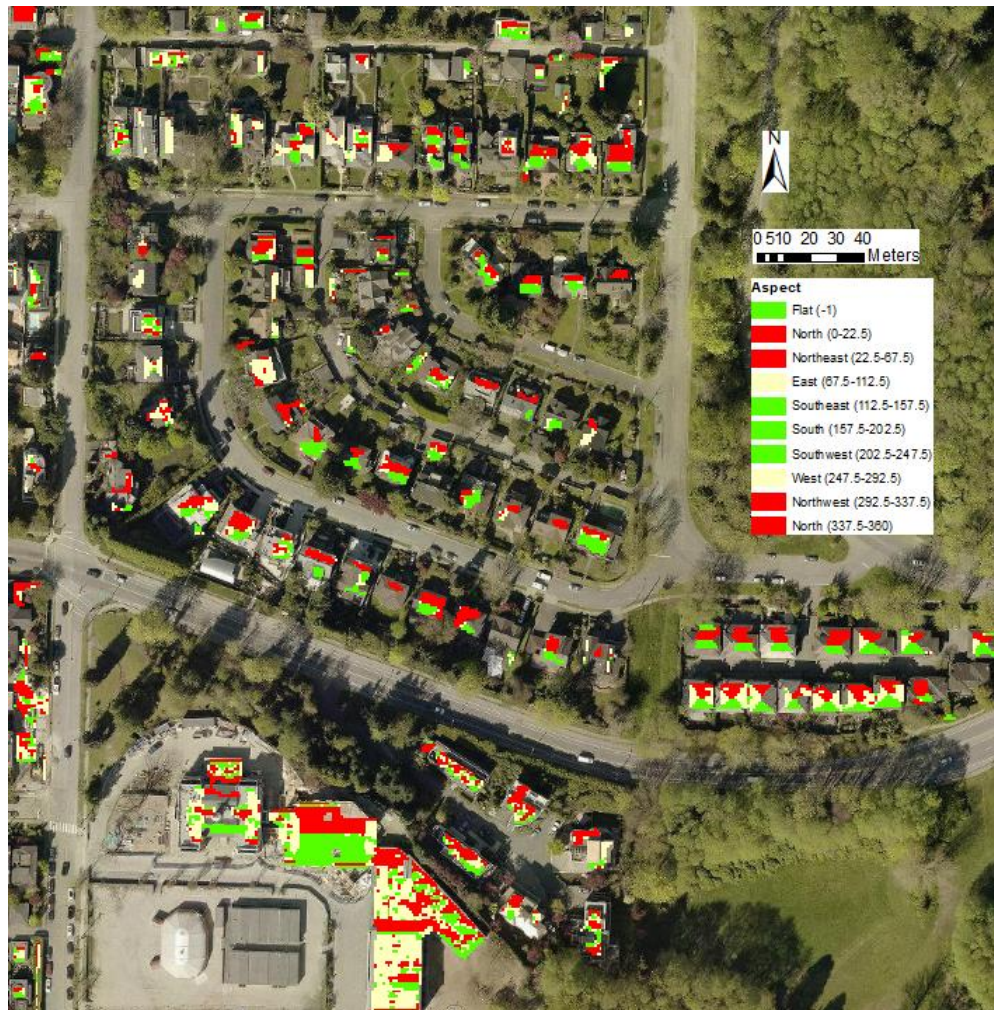


Figure 3.3-4 Aspect Calculated from the DSM Raster

As mentioned in Section 2.3, north-facing roofs are not efficient for receiving solar radiation in the northern hemisphere. Although most north-facing roofs (aspect from 0 to 67.5 and from 292.5 to 337.5) were successfully identified in ArcMap, protruding objects on a flat

roof resulted in erroneous aspect values. This was addressed by using Zonal Statistics in ArcMap, which assigned the majority aspect values to a roof polygon containing the raster cells. The raster data was then converted to polygons, which were roof polygons with aspect values. The roof polygons with unsuitable aspect values (north-facing) were removed, and the remaining polygons were considered to have suitable orientations to install solar panels.

Third, roof slope was considered. Previous studies found that roof slope over 60° is unsuitable for PV panel installation (Boz et al., 2015; Jakubiec & Reinhart, 2013). To account for this, the original DSM was clipped to the aspect-suitable polygons, and their slope was calculated using the Slope tool. Zonal Statistics then associated each roof polygon with the majority slope value within it. The raster was converted to polygons, and those with slope values above 60 degrees were removed. An alternative approach to using a defined threshold is to show the slope values in a color gradient.

The remaining polygons are the final output, the suitable roofs. Their shape area were calculated in the attribute table. The available roof area was compared to the area of the roof containing the suitable roof polygons. This was done by spatially joining the suitable roof polygons to the building footprint polygons containing them using the “CENTER IN” match option.

3.4 Energy Output Potential

In this step, annual ground solar radiation was calculated in Section 3.1.2, average solar panel efficiency was determined by land surface temperature in Section 3.2.2, and available roof area was obtained in Section 3.3.2. A 50% solar panel coverage was assumed in this project, and the energy output potential is estimated using Equation 3.4.

Energy output potential =

received solar radiation * solar panel efficiency * available roof area * solar panel coverage

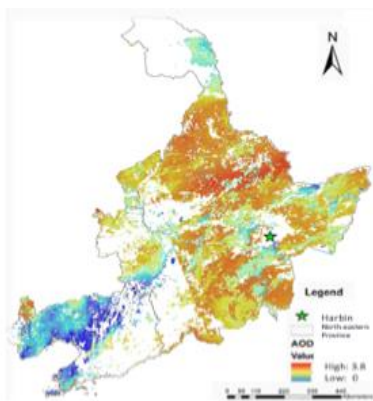
equation 3.4

Chapter 4. Results

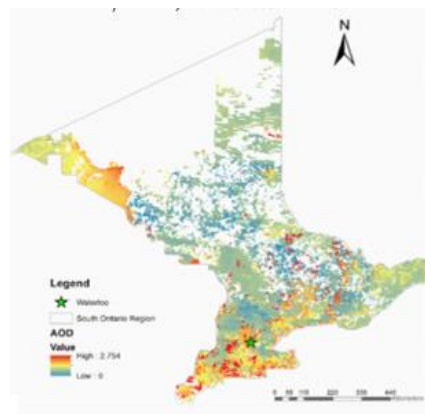
4.1 Air Pollution

This section describes the results related to average AOD value of three study areas and the loss of solar radiance within the most suitable study area. Specifically, Section 4.1.1 displays the annual AOD value for three study areas. Section 4.1.2 shows the seasonal variation of AOD value in one selected study area. Section 4.1.3 demonstrates the loss of solar radiance of one selected city owing to the air pollution. Section 4.1.4

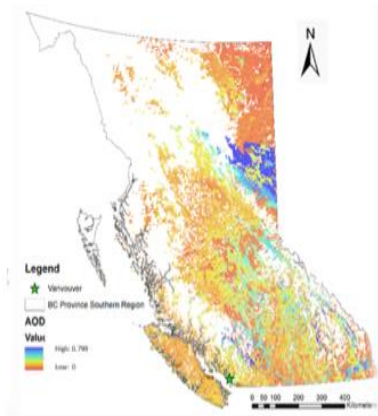
4.1.1 Annual AOD for Three Provinces.



a) Northeastern Province, China



b) Ontario, Canada



c) British Columbia, Canada

Figure 4.1-1 Annual AOD in three provinces

Annual AOD for three provinces are shown in figure 4.1.1, the aerosol optical depth data is collected from 2013 to 2017 to analyze the AOT value for our study areas. Using stratified sampling for every month, we select one day at each air quality level (good, moderate, and unhealthy) to represent the average aerosol optical thickness. We select the AOT product data at 12pm when the AOT value can represent the average value of the entire day (Mintz, 2009). Owing to the cloud mask, there are some areas without AOD value in northern part of BC province.

Different land cover may have different AOD values. For northeastern province in China, it can be found that major high AOD values are concentrated in the northern part, where large quantities of chemical plants are located. In addition, the regions covered by forest have the relatively less AOD value in the centre of the province. As for Ontario, generally, the total AOD value is better than that of region in China. The regions which have the most air pollution are mainly in the southern and eastern part of the region. It can be concluded that the region closed to sea and with several creeks or rivers may have relatively larger AOD value, owing to the impact of the vapour on the image and the accuracy of the algorithm. In British Columbia, it can be found that the AOD value is closely associated with the population density and the location of the factories. Since there are less residents living in northern part of BC province, there are little AOD data in northern part of BC province. In addition, the regions with larger AOD values are mostly with higher population density and more factories, which may produce more pollutant.

Specifically, the average AOD values in three provinces are different. The northeastern province in China has the largest AOD average values of 1.5, indicating the most air pollution. The British Columbia is the province with the least AOD average value of 0.46, which illustrates the least air pollution in this region.

Since that Aerosol Optical Thickness (AOT) one of the most important component in the atmosphere, which can quantitatively measure the loss of solar radiation due to aerosol scattering and absorption between the point of observation and the top of the atmosphere (Aloysius et al., 2008). AOT is another consideration to assess the suitability for photovoltaic development over a large geographic scale. Smaller AOT value indicates less loss of solar radiation, which can guarantee the abundant solar resource. In provincial level, the British Columbia province seems to be the most suitable province with relatively least loss of solar radiation owing to air pollution.

4.1.2 Seasonal Aerosol Optical Depth within One City

Since aerosols are one of the greatest sources of uncertainty in climate modeling, it varies in seasons and spaces. It is of significance to study the AOD's variation through seasons. Figure 4.1-2 shows the different AOD distribution in four seasons in Vancouver.

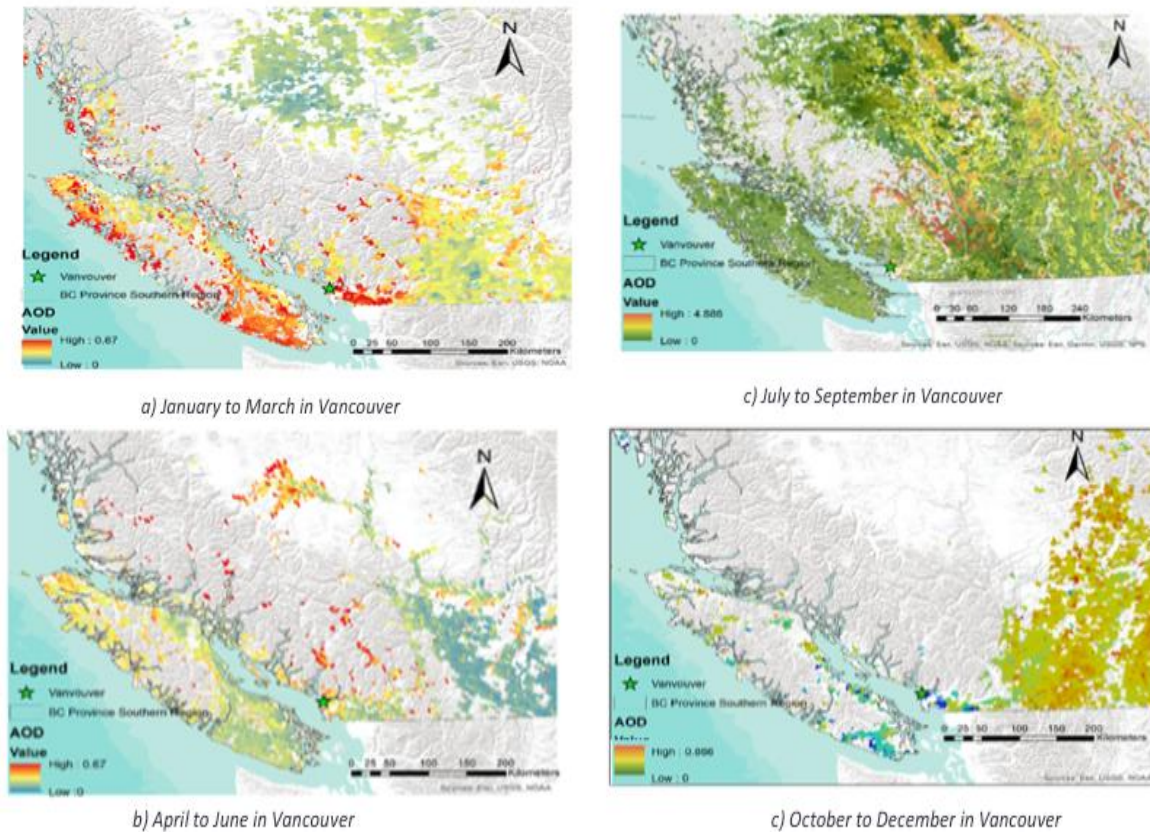


Figure 4.1-2 Seasonal Aerosol Optical Depth map in Vancouver

It can be seen that different seasons have different value and distribution of AOD, which indicates different air pollution condition. Generally, in summer, the AOD values are dramatically larger than other seasons, which may be owing to the temperature and frequent events of factory. In addition, it can be concluded that the region next to sea has the relatively large AOD value

4.2 Land Surface Temperature

This section describes the results related to land surface temperature and solar-efficient areas within one city. Specifically, Section 4.2.1 demonstrates the annual land surface temperature for three cities. Section 4.2.2 shows the monthly land surface temperature in one selected city. Section 4.2.3 presents the solar-efficient areas by considering urban heat island and

solar panel operating efficiency. At the end, Section 4.2.4 describes the final selection of the city tiles for further three-dimensional modeling.

4.2.1 Annual Land Surface Temperature for Three Cities

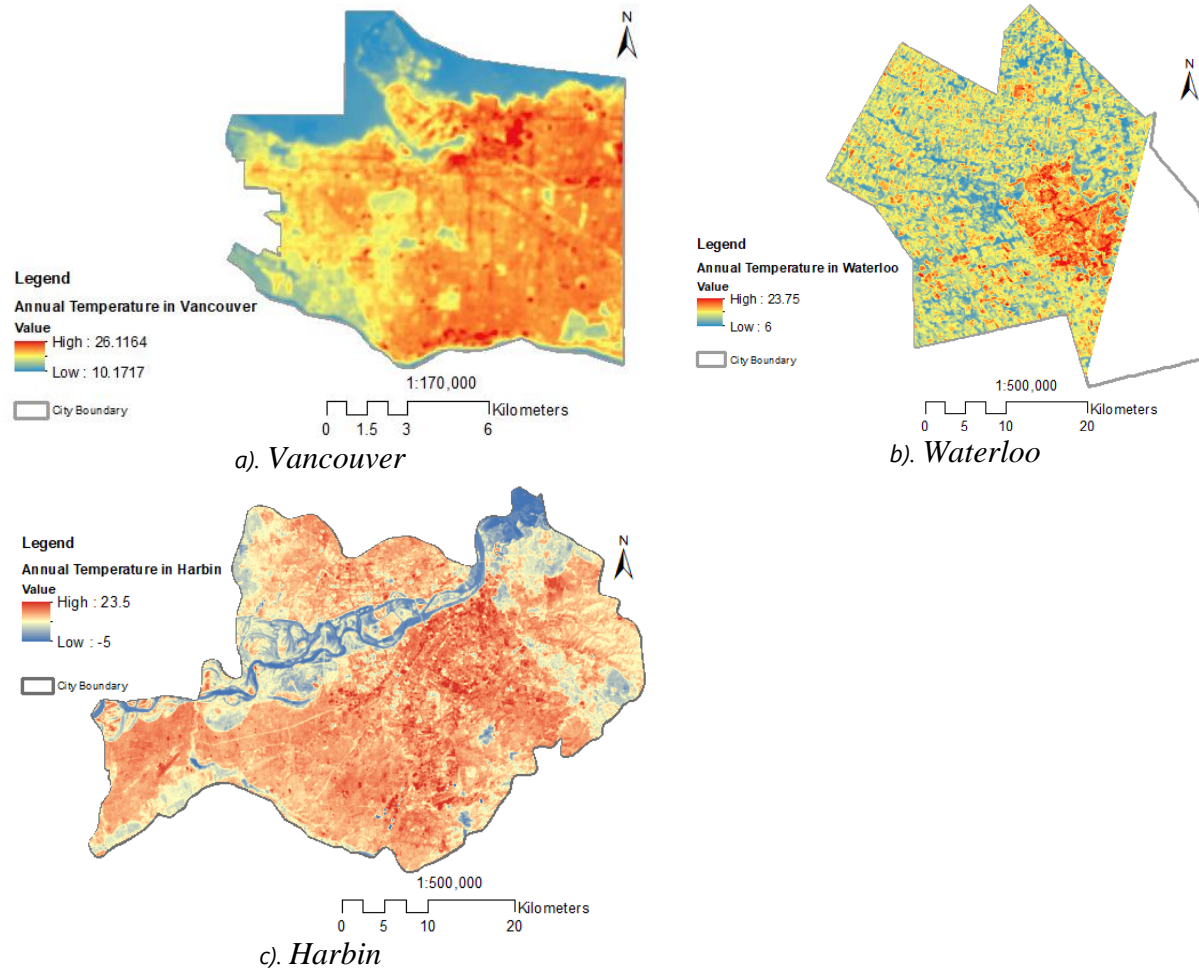


Figure 4.2-1. Annual Land Surface Temperature in Study Area

Annual land surface temperature for three cities are shown in Figure 4.2-1. Landsat 8 images were collected from Jan 2013 to Dec 2014. Due to cloud masks, most satellite images are not qualified. Thus, this project only collected four seasonal satellite images for Waterloo and Harbin individually in order to calculate the average land surface temperature. In Vancouver, most Landsat 8 images are not masked by clouds, so monthly data were collected for Vancouver.

Difference land surface features show different temperature. Most high surface temperature areas (shown as dark red) are distributed in urban areas: the northern part of the City of Vancouver, the center part of Kitchener-Waterloo (KW) Region, and the southern part of Songhua River. Consistent with the research from Kikon et al. (2016), the results in this project reflect the effects of urban heat island. Urban areas are usually warmer than suburban areas due to human activities and greenhouse gas emissions. In addition, natural environments exert an importance influence on local temperature due to atmospheric effects and ocean movement. Hence, there is a large difference in surface temperature for the three cities, which almost locate in the same latitude. Comparatively, water and vegetation show the relative low annual surface temperature (shown as blue) in Vancouver Harbour, suburban areas of KW Region, as well as Songhua River. Urban heat island and high specific heat capacity of water affects this distribution of land surface temperature.

Specifically, the annual surface temperature differs in three cities. Harbin shows the coldest temperature from -5 to 23.5 °C, followed by Waterloo (6 to 23.75); the warmest one is Vancouver, whose surface temperature ranges from 10.17 to 26.11. As mentioned before, the effects of cloud masks make the data collection difficult, this project only select the seasonal satellite images for Harbin and Waterloo. Their surface temperature shows slightly higher than the historical temperature collected from weather station (Figure 1-2). For the City of Vancouver, the annual surface temperature is quite consistent with the historical temperature.

In order to select one city within the most solar-efficient potential, land surface temperature is a curtail factor. As mentioned before, solar panels tend to have higher efficiency in cold weather because the ambience helps to cool the operating system. Technically, Harbin should be considered as the best, but snow is another important factor. According to Mani and

Pillai (2010), snow accumulation causes a large amount of energy loss when solar light passes through snowpack. Thus, covered by snow for almost half year, Harbin is not suitable for installing solar panels. Waterloo experiences the same limitation caused by snow. Thus, Vancouver is selected for further analysis.

4.2.2 Monthly Land Surface Temperature within One City

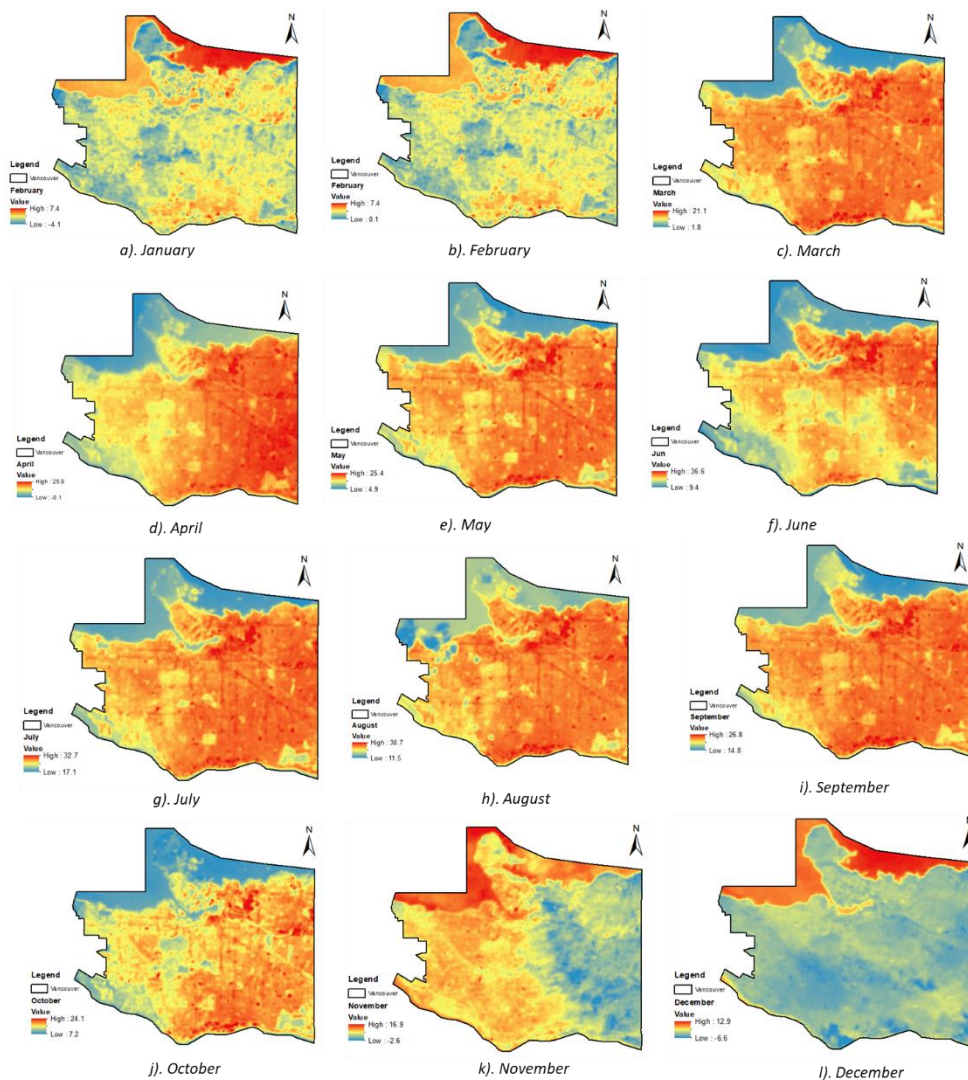


Figure 4.2-2. Monthly Land Surface Temperature in Vancouver, BC

Monthly land surface temperature in the City of Vancouver is shown in Figure 4.2-2.

Landsat 8 images were collected from Jan 2013 to Dec 2014. Since most satellite imagery are

limited by cloud masks and incomplete cover on the study area, this project only selected one representative image in each month.

The results show that monthly distributions of land surface temperature are changed regularly. For water body, which is shown in the north part of the city, its surface temperature shows higher temperature than the urban area in January and February. From March to October, as temperature rises, the entire surface temperature in water body increase but is relatively lower than the surface temperature in the urban area. In the winter season, the overall surface temperature of water body decreases again but is relatively higher than the urban area decreases again but shows the higher than that of the urban area again. The maximal surface temperature of water body is 17.1°C in July while the minimal is -0.1°C in April. The regular change in water surface temperature are caused by the high heat capacity of water, which decides water need more energy to increase its temperature than other land features (Giauque & Stout, 1936). In the urban area, the changes in its land surface temperature are greater than water body. In winter seasons (November to February), the land surface temperature is relatively lower than water, -4.1 and 0.1 respectively. In other seasons, with the increase in air temperature, the surface temperature in urban area also increase and shows a greater change in the difference of maximal and minimal temperature. The maximal surface temperature in the urban area is 36.6°C in June while the minimal is -6.6°C in December.

The effects of urban heat island are reflected in the monthly surface temperature. As mentioned in the literature review chapter, human daily activities can cause the metropolitan area warmer than suburban area (Stone & Rodgers, 2001). It is notable that several regions with high building density in the north part of the city is reflected by the dark red. This area is near the Vancouver Harbour and has a large number of high-rise buildings. In addition, several major

road lines also show the higher temperature than other areas. Consistent with the effects of urban heat island, these areas with high population or commuting density are relatively warmer than other areas. In the summer season (May to September), the average surface temperature near the Vancouver harbour is about 30°C.

4.2.3 Solar-Efficient Areas within One City

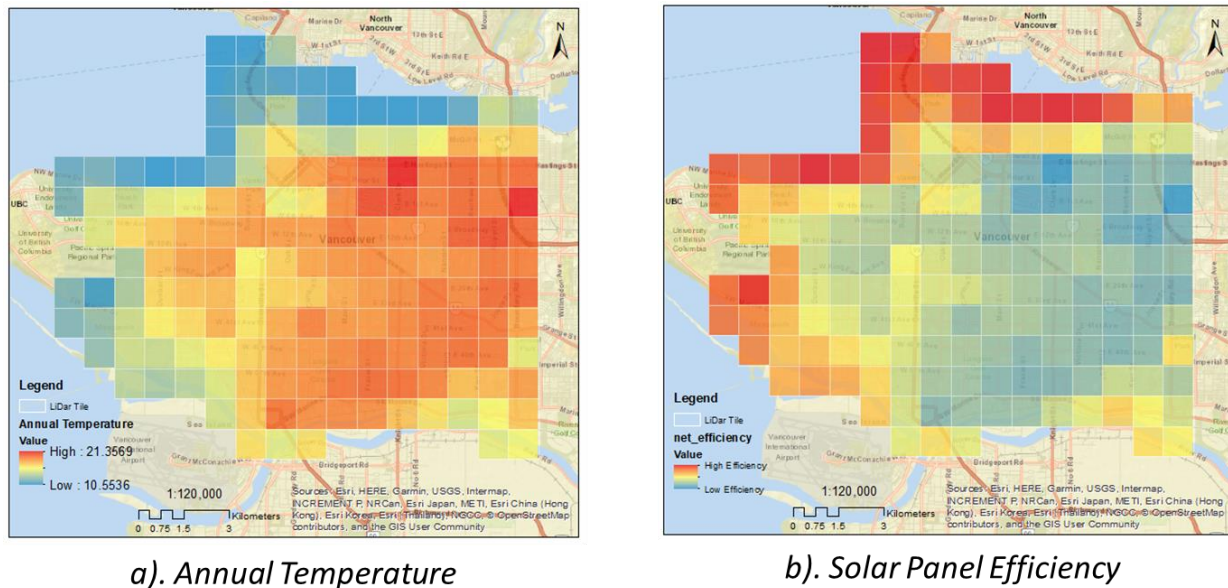


Figure 4.2-3. The Estimated Solar Panel Efficiency Based on Annual Temperature

The estimated solar panel efficiency within the City of Vancouver is shown in Figure 4.2-3. Since the hot temperature can influence the cooling system in solar panels and reduce the final power output, the areas with hot temperature is not suitable to install solar panels. The left figure in Figure 4.2-3 demonstrates the annual temperature within the LiDAR tiles while the right one shows the estimated solar panel efficiency by employing the linear transformation. It is notable that the higher the land surface temperature (red color in the left), the lower the estimated solar efficiency (blue color in the right).

Most high solar-efficiency areas (red color in the right) are distributed near the city boundary due to less effects of urban heat island. In particular, the area near the water shows the

relatively high solar-panel efficiency, about 16%. In comparison, the net efficiency in urban areas is less than 15%. While the numeric difference between high and low efficiency is not a large number, only 1%, the unit of efficiency is the percentage, which means the annual energy loss of 1% is a huge loss. Considering the effects of urban heat island can lead to a more accurate estimation of annual power distribution.

4.2.4 Final Selection of City Areas

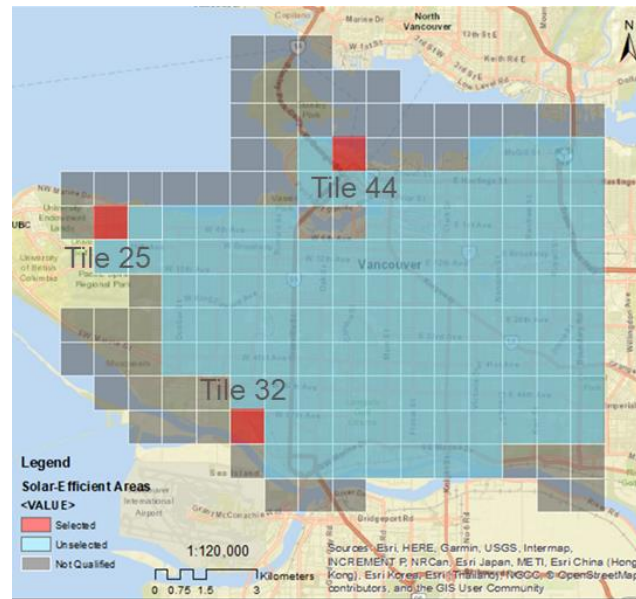


Figure 4.2-4. The Final Selected Tiles for Solar Panel Installation

The final selected tiles with the highest solar panel efficiency is shown in Figure 4.2-4. Some tiles, while have largest solar panel efficiency, locate on the water or parks where no building exists. Thus, these tiles are first filtered out (shown as gray color). From the rest of tiles, the top three (shown as red color) were selected, which are Tile 25, Tile 44, and Tile 32. The tiles labeled blue are suitable for solar panel installation but are not the most solar-efficiency areas. The average solar efficiency in these three tiles is 15.5%, which are used to further evaluate the suitable values of each building in the next section.

4.3 Suitable Roofs

Building footprint polygons were extracted from the LiDAR data (Figure 4.3-1), and they were divided into roof polygons based on the difference in surface elevation. Figure 4.3-2 shows an example of the initial roof polygons (colored by shape area), and the final suitable roof polygons (colored by shape area). In this residential area, the project effectively identified the suitable roofs considering rooftop structure, tree canopies, aspect, and slope. A building may be large in footprint while small in suitable roof area.



Figure 4.3-1 Building Footprints in the Three Selected Tiles



Figure 4.3-2 Roof Polygons to Suitable Roofs

Figure 4.3-3 shows the identified suitable roof in the three selected areas. The residential areas provides less suitable roofs than the commercial area as the residential roofs are smaller and usually comprise north-facing or steep roofs. Although commercial buildings tend to be flat-roofed, some of their roofs are occupied by heating and ventilation facilities. From left to right, the total suitable roof areas are 25877 m², 227249 m², and 36571 m².



Figure 4.3-3 Suitable Roofs

4.4 Daily Energy Output

Air pollution considerably impacts ground-level solar radiation. Vancouver tops the three cities in solar resources at 3.45 KWh/m²/day. Spatial variation in surface temperature is significant within Vancouver. Annual solar cell efficiency is 15.5% in the coolest parts of the city. Suitable roofs abound in the city, with commercial area having much higher PV potential than residential neighborhoods. With a 50% solar panel coverage on the suitable roofs, the considered areas (Tile 25, 32, and 44) are expected to generate 6.9 MWh, 60.8 MWh, and 9.8 MWh per day respectively. Figure 4.4 shows the suitable roofs colored by their energy output potential.



Chapter 5. Discussions

This section discusses the project results. Section 5.1 assess the accuracy of the outputs and Section 5.2 reflects on the limitations and improvements.

5.1 Assessment of Results

5.1.1. Air Pollution

Accuracy will be assessed using ground-based measurement. The validation data is the surface AOT data from spectrophotometer provided by AERONET's aerosol measurement networks. Based on the space-time matching methods, the accuracy of AOT value from MODIS product can be assessed through the following steps. (1) Select 5×5 grids (10 km * 10 km per grid) which use AERONET observation sites in Waterloo, Vancouver and Harbin as the center. (2) Select the corresponding ground data observed from AERONET within 30 minutes before and after the satellite transit, during which there are usually 4 or 5 observations. Specific statistics also requires that MODIS data have at least 5 grid points in every 25 grids, equivalent to an area of 50 km * 50 km. The space-time matching will fail if there are fewer than two observations within 30 minutes before and after the satellite transit. (3) After comparing the surface value of AOD and the average value from MODIS product, the accuracy of the AOT product will be produced. Table 5.1.1-1 is the plot of minimum, maximum, mean and surface data of AOD.

Table 5.1.1-1 The Loss of solar radiance owing to air pollution in Vancouver

Average AOD in Vancouver	Solar Radiation	Loss of solar radiation	Percentage of loss
0.46	4.3125kwh/m ² /day	0.8625 kwh/m ² /day	20.09%

5.1.2 Land Surface Temperature

To evaluate the accuracy of the estimated land surface temperature, the air temperature were collected from weather stations. Considering the difference between surface temperature and air temperature, this project also used other two methods to evaluate the results. The first method is to estimate the land surface temperature without considering the atmospheric effects. Specifically, according to Jiménez-Muñoz and Sobrino (2003), the surface temperature can be directly transformed from the solar radiance using the Planck's Law. Another method is an improved NDVI Threshold method by considering heterogeneous surface emissivity (Chen et al., 2015). Since there is no other data source that can provide free surface temperature, the air temperature from weather stations are considered as the "Ground Truth" to evaluate the results in this project.

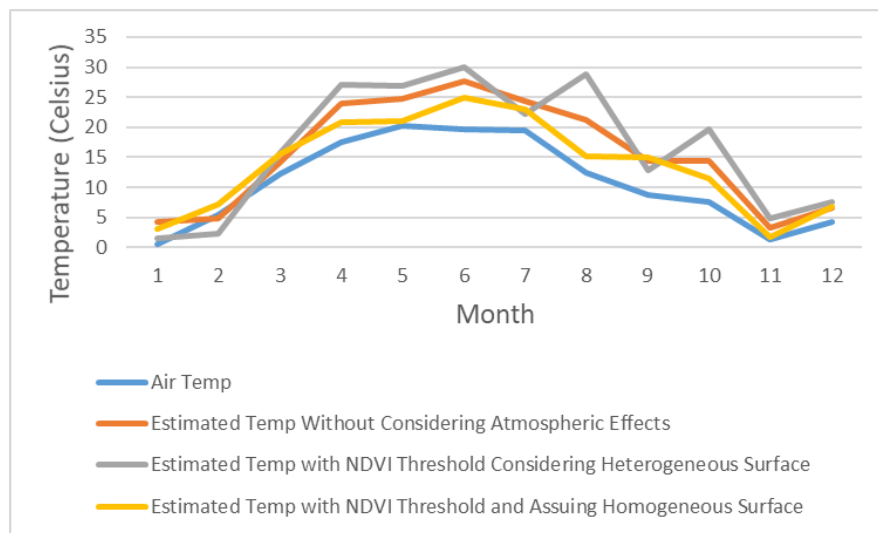


Figure 5.1.2-1 The Comparison between Air Temperature and Three Estimated Temperature

The monthly temperature from weather stations and three methods are shown in Figure 5.1.2-1. It is notable that the estimated temperature by using NDVI Threshold method and assuming the homogeneous surface (yellow line) is closest to the air temperature. While the direct estimation without considering the atmospheric effects (orange line) has a similar trend

with the air temperature, the difference between two results are large. The results by considering heterogeneous surface (grey line) are not qualified due to the apparent changes occurring from August to November. Thus, the method used in this project are closest to the air temperature.

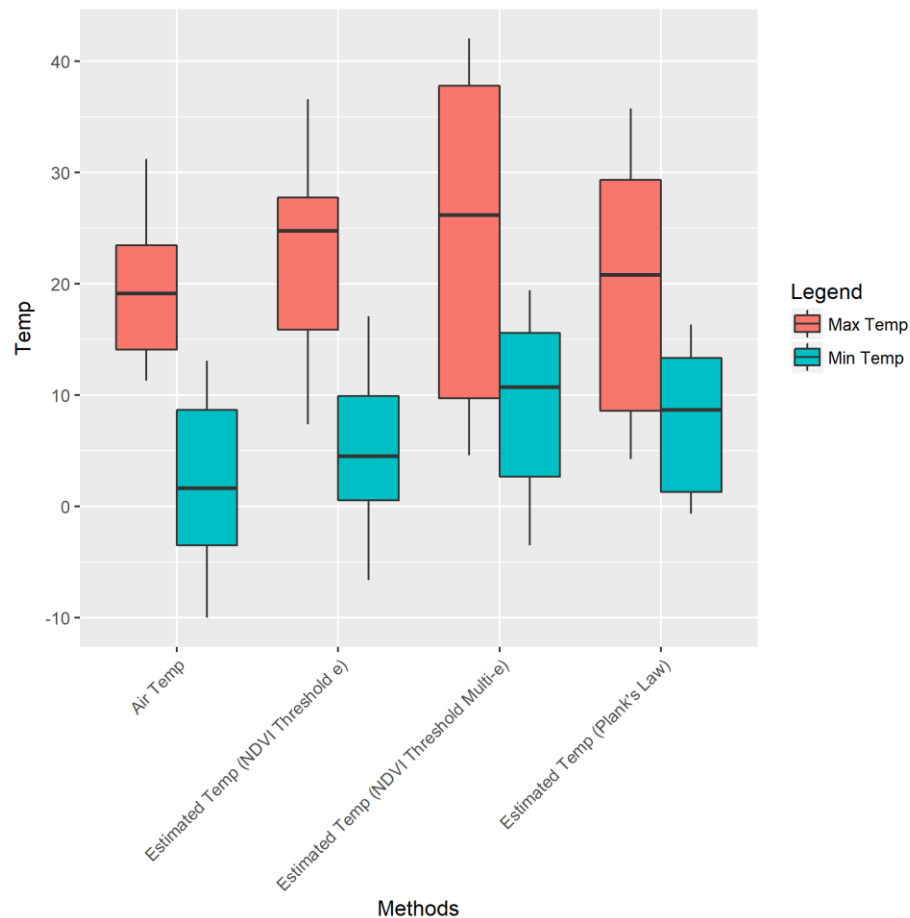


Figure 5.1.2-2 The Comparison between Three Methods in Maximal and Minimal Temperature

The statistical information about three methods and air temperature is shown as a boxplot in Figure 5.1.2-2. Consistent with the line chart, the methods by considering heterogeneous emissivity (the third group) has the largest rectangle, reflecting the largest standard deviation. Thus, the estimated values using this method have a large difference with the average temperature. The direct estimation using the Plank's Law (the last group) also have a large standard deviation, compared with the NDVI Threshold method only considering a

homogeneous emissivity (the second group). In terms of the distribution of estimated surface temperature, the method used in this project are closer to the air temperature.

Table 5.1.2-3 The Statistical Results between Three Methods

	Estimated Temp Directly		NDVI Threshold Considering Heterogeneous Emissivity		NDVI Threshold Considering Homogeneous Emissivity	
	Minimal Temp	Maximal Temp	Minimal Temp	Maximal Temp	Minimal Temp	Maximal Temp
MAE	5.581	5.458	6.885	8.545	3.133	3.967
RMSE	6.507	6.130	7.764	10.435	3.523	4.512

The assessment of three methods are shown in Table 5.1.2-3. The Mean Absolute Error (MAE) and Root Mean Square Error (RMSE) are calculated based on the air temperature. It is notable that the NDVI method that assumes the homogeneous emissivity has the lowest MAE (3.133 for minimal temperature and 3.967 for maximal) and RMSE (3.523 for minimal temperature and 4.512 for maximal). These statistical values indicate that the average estimation error in this methods is the lowest. In comparison, the NDVI method that considers heterogeneous emissivity shows the largest errors in terms of MAE and RMSE, while the direct estimation without considering the atmospheric effects are the second best. One possible explanation why the accuracy decreases when considering the heterogeneous emissivity is that the empirical parameters used in the method are not suitable for Vancouver. Different surface features have different emissivity so it is quite difficult to obtain accurate results without in-situ parameters. In addition, the atmospheric factors show the strong influence on estimating land surface temperature. Without considering the atmospheric effects, land surface temperature cannot be accurately estimated.

After comparing with the air temperature and two methods, the method used in this project shows the best accuracy. The atmospheric effects exert important influence on the estimation of land surface temperature; using empirical parameters show the negative impact on retrieving land surface temperature. Comparatively, the method, that reduces the atmospheric

effects and assumes the homogeneous emissivity, shows the best accuracy: the trend closest to air temperature, low standard deviation, as well as low MAE and RMSE. Thus, the results in this project is statistical convincing and can accurately reflect the solar panel efficiency in order to estimate the power output.

5.1.3 Suitable Roofs

Figure 5.1.3 plots the area of building footprint (x-axis) against the area of suitable roofs (y-axis). It shows that most buildings in the selected areas are smaller than 250 m² in foot print, and the area of suitable roof tend to be half of the building size. Points falling on the diagonal line suggests the buildings whose suitable roof area equals to the building roof area. However, the points above the diagonal line near the y-axis indicate that a small number of the small buildings have a suitable roof area larger than the building footprint. This is an error caused by converting raster to polygons which identified neighboring raster into one polygon. Thus the area of the connected suitable roof polygons surpassed the area of the buildings containing their centers.

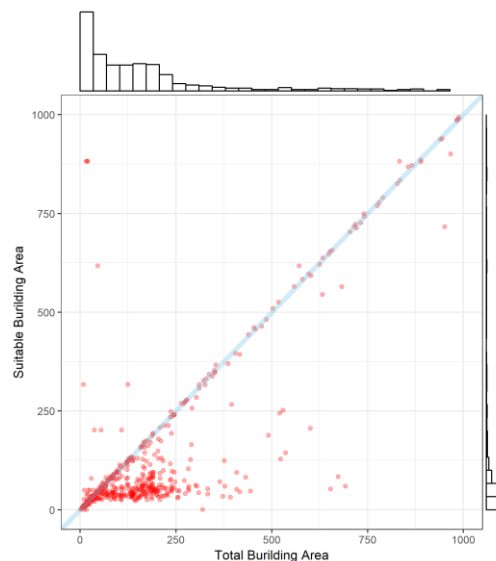


Figure 5.1.3 Suitable Roof Area Compared to Building Area

5.2 Limitations

5.2.1 Limitations in Assessing Air Pollution

Specific wavelength used for retrieving AOD value is one of the most important factors in estimating Aerosol Optical Depth. Since the algorithms used in MODIS product to calculate AOD value is based on red and blue band, the AOD values acquired in MODIS product is the specific value in red and blue band. However, there exist variations of AOD value in different wavelengths. It is better to identify which frequency or range of wavelength is suitable for photovoltaic system and retrieve the corresponding AOD value of the specific wavelength.

Expect for the loss of solar radiation owing to the scatter and diffuse of the aerosol particles, the microscope particles dropping on the solar panels may have a relative impact on the efficiency of solar panels. The density of the dirt or microscope particles on the solar panels can influence the panels to capture solar radiation and convert it to electricity efficiently. It is significant to study the relationship between the dust density and solar panel efficiency. In addition, retrieving the relationship between the AOD value and the dust density may require the wind speed and wind direction and other climate factors, which can be improved in the further research.

5.2.2. Limitations in Estimating Land Surface Temperature

Atmospheric effect is one of the most important factors in estimating land surface temperature. According to Zhao et al. (2010), the Single Window is quite sensitive to the content of water vapor because it can cause a significant attenuation of atmospheric transmission. Compared with the other two cities, Vancouver, near the ocean, is the one with the largest amount of water vapor every year (World Weather Online, 2018). As a result, there is a great difference between the temperature estimated by algorithms and the temperature from ground

weather stations. From the monthly results in previous section, it is notable that the estimated maximum temperature is quite large. One possible explanation is that on hot days, a large amount of water vapor evaporates from the ocean. Although this project has utilized the atmospheric parameters (upwelling and downwelling radiances) to alleviate the influences of water vapor, the overall accuracy is still limited by these general parameters. Future studies should collect in-situ atmospheric profiles to retrieve more accurate land surface temperature.

Emissivity effect is another important factor in estimating land surface temperature. Emissivity is dependent on the surface composition, moisture, as well as roughness, so the estimation process is limited by heterogeneous features (Sobrino et al., 2008). In this project, NDVI Threshold method was employed to estimate emissivity. Compared with some methods that neglect the emissivity effects, the NDVI Threshold method can accurately extract the emissivity of vegetation. One limitation existing in this method is that the emissivity of the urban area was estimated by using the empirical parameters. In addition, the heterogeneous surface features limit the accuracy in this project. From the assessment, while the heterogeneous surface features are considered, the results are not encouraging. The major issue is that the empirical parameters are used. Future study should consider obtain in-situ emissivity to improve the estimation of land surface temperature.

Additionally, lacking ground truth data is a great issue in this project. As mentioned before, the urban heat island effects cause the different temperature distribution within one city. There is no access to the in-situ ground truth data, so this project collected the historical temperature as the validation data. However, the validation data is also influenced by the urban heat island, and more importantly, the temperature data from weather stations reflect the air temperature rather than the land surface temperature. Thus, the estimated temperature shows

great difference with the validation data. It is difficult to exactly measure the accuracy of the methods used in this project, but the overall accuracy is still promising. Future studies should collect more accurate ground truth data to validate the results.

5.2.3 Limitations in Identifying Suitable Roofs

ENVI LiDAR algorithms to extract building polygons and DSM were not explained, and it is difficult to assess the accuracy of the output. Referring to Figure 5.2.3-1, most of the identified large and wide roof polygons were shifted from the base map satellite image, and the edges did not match the buildings precisely. It is difficult to accurately extract the surface of a small area from LiDAR data as the point density is limited to represent the edges and other details.



Figure 5.2.3-1 Issues with the Identified Large Roof Polygons

This project classified roof polygons by area in quantiles to remove the identified small roof areas that are likely to be different in elevation due to the occupation of tree canopy or rooftop structures. However, the project used strict thresholds (over 20 m² and different for each tile) to remove 60% to 70% of the identified roof polygons. This approach may have failed to

account for the small roof areas that are suitable for solar panels, but it gives priority to larger roofs for installation and maintenance conveniences.

The ArcMap Aspect tool hardly identified a roof as flat. It is possible that most buildings are sloping in a small angle, but a more likely reason is the small rooftop structure with a different elevation from the roof surface. The Slope tool was also subject to this error caused by the “noise objects” projecting from the roof surface. Calculating the majority aspect or slope value using the Zonal Statistics tool helped to identify the aspect and slope of a roof polygon, but the edges of the raster did not perfectly match the roof polygon boundaries.

Another defect lies in converting raster to integer values and then vector polygons. This was done after using Zonal Statistics to show the suitable roof polygons. The aspect and slope values initially contained one decimal digit, so converting to integers did not affect significantly. Referring to Figure 5.2.3-2, roof polygons converted from raster cells usually fell within the initial roof polygons. This reduced the overall estimated suitable area but acted as a consideration to avoid installing solar panels close to the roof edges. A small number of nearby raster cells were merged into one polygon as mentioned in Section 5.1.3.

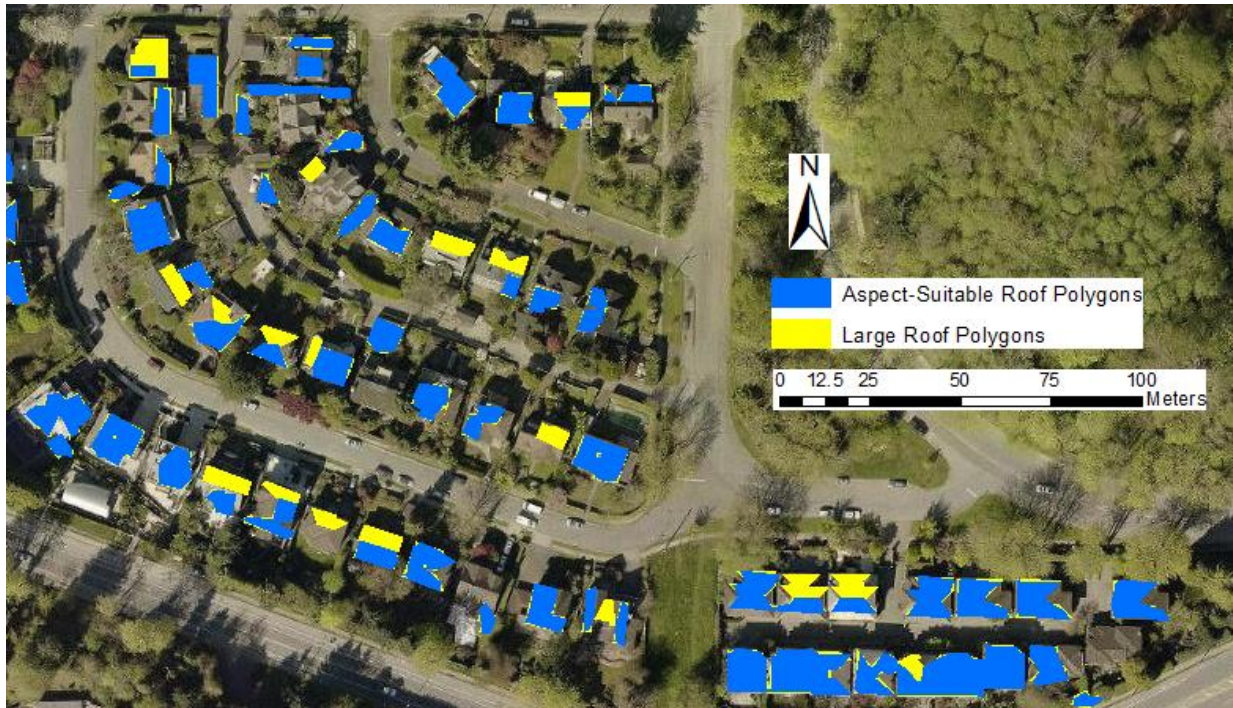


Figure 5.2.3-2 Issues with Converting Raster to Polygons

5.2.4 Limitations in Calculating Daily Output

The output efficiency of solar panels depends on the surface temperature, the types of solar cell, the entire operating system, as well as the embedded cooling technology (Dubey et al., 2013). It is quite difficult to determine which energy conversion parameters (equations) are better. In this project, a set of widely used parameters is selected to measure the energy loss in different temperatures. According to Dubey et al. (2013), these parameters can only estimate a general efficiency of solar cell. In addition, it is possible that recent technology development has improved the solar panel system and the previous parameters may be not suitable. Thus, future studies are suggested to collect the latest parameters about the energy conversion in certain type of solar cells.

The project assumed a solar panel coverage at 50% on the suitable roofs. Future studies can look into suitable coverage ratios for different types of roofs. The project did not consider the shading from nearby building as it changes during the day. Other factors affecting solar panel output such as air pollutant cover and maintenance costs were not considered.

Chapter 6. Conclusions

The project fulfills the four research objectives. It fosters the progress towards the 7th United Nations Sustainable Development Goal by encouraging policy commitment and acceptance of distributed photovoltaic systems. It informs administrations and communities of the suitable building roof for which they can provide political and financing incentives.

In response to Objective 1, In response to Objective 1, this project retrieved the AOD in order to estimate the loss of solar radiation owing to the air pollution. Comparing the different AOD value, the most suitable province with the least air pollution can be selected. An annual solar radiation loss is estimated in Vancouver, BC, reducing the radiation to 3.45 KWh/m²/day.

In response to Objective 2, this project retrieved the land surface temperature in order to estimate the solar panel efficiency. Since the solar panel efficiency is negatively related to the surface temperature, Waterloo and Vancouver are more suitable to solar panel installation than Harbin. After considering the energy loss caused by snow accumulation on solar panels, Vancouver was finally recommended to this project. Monthly surface temperature in Vancouver reflects the effects of urban heat island, presenting the different distribution of surface temperature within one city. The solar-efficient areas are estimated by using the annual temperature and the linear transformation from temperature to net efficiency. The final selected tiles are near the sea or parks, with the average solar panel efficiency of 15.5%. The major limitations in this project come from the atmospheric effects, lack of “ground truth” surface temperature, as well as empirical parameters for homogeneous emissivity.

In response to Objective 3, the project identified suitable building roofs in three thermal-efficient 1 km² area in Vancouver. The roof areas occupied by facilities or covered by tree canopies were excluded, and roofs facing north or steeper than 60 degrees were removed.

Commercial areas have higher photovoltaic potential than residential neighborhoods because commercial buildings tend to be larger in size and more suitable in roof slope. The total suitable roof areas are 25877 m², 227249 m², and 36571 m² (tile order in Figure 4.3-3). Limitations came from the uncertainty in extracting roof polygons from LiDAR data and the conversion from raster data to vector polygons.

In response to Objective 4, daily energy output was calculated using ground-level solar radiation, solar cell efficiency, and suitable areas obtained from completion of the objectives above. Assuming a 50% solar panel coverage on the suitable roofs, the three areas (tile order in Figure 4.3-3) are expected to generate 6.9 MWh, 60.8 MWh, and 9.8 MWh per day respectively. Future studies can individualize the solar panel coverage for different roofs and consider other factors for solar panel efficiency.

References

- Aguirre, M., & Ibikunle, G. (2014). Determinants of renewable energy growth: A global sample analysis. *Energy Policy*, 69, 374-384.
- Akikur, R. K., Saidur, R., Ping, H. W., & Ullah, K. R. (2013). Comparative study of stand-alone and hybrid solar energy systems suitable for off-grid rural electrification: A review. *Renewable and Sustainable Energy Reviews*, 27, 738-752.
- Alexander, C., Smith-Voysey, S., Jarvis, C., & Tansey, K. (2009). Integrating building footprints and LiDAR elevation data to classify roof structures and visualise buildings. *Computers, Environment and Urban Systems*, 33(4), 285-292.
- Atmospheric Correction Parameter Calculator. (2018). [website]. Retrieved from: <https://atmcorr.gsfc.nasa.gov/>.
- Balçık, F. B. (2014). Determining the impact of urban components on land surface temperature of Istanbul by using remote sensing indices. *Environmental monitoring and assessment*, 186(2), 859-872.
- Baldocchi, D., Falge, E., Gu, L., Olson, R., Hollinger, D., Running, S., ... & Fuentes, J. (2001). FLUXNET: A new tool to study the temporal and spatial variability of ecosystem-scale carbon dioxide, water vapor, and energy flux densities. *Bulletin of the American Meteorological Society*, 82(11), 2415-2434.

- Becker, F. (1987). The impact of spectral emissivity on the measurement of land surface temperature from a satellite. *International Journal of Remote Sensing*, 8(10), 1509-1522.
- Begum, S. F., Islam, M. R., Yamaguchi, Y., & Ogawa, K. (2003). Studies on Surface Temperature using Remote Sensing Technique in the NW Part of Bangladesh. *Geocarto International*, 18(3), 41-49.
- Bergamasco, L., & Asinari, P. (2011). Scalable methodology for the photovoltaic solar energy potential assessment based on available roof surface area: Application to Piedmont Region (Italy). *Solar Energy*, 85(5), 1041-1055.
- Boz, M. B., Calvert, K., & Brownson, J. R. (2015). An automated model for rooftop PV systems assessment in ArcGIS using LIDAR. *AIMS Energy*, 3(3), 401-420.
- Caselles, V., Coll, C., Valor, E., & Rubio, E. (1997). Thermal band selection for the PRISM instrument: 2. Analysis and comparison of existing atmospheric and emissivity correction methods for land surface temperature recovery. *Journal of Geophysical Research: Atmospheres*, 102(D16), 19611-19627.
- Chakraborty, S. D., Kant, Y., & Mitra, D. (2015). Assessment of land surface temperature and heat fluxes over Delhi using remote sensing data. *Journal of environmental management*, 148, 143-152.
- Chen, J., Yang, K., Zhu, Y., & Su, F. (2015, June). Analysis of the relationship between land surface temperature and land cover types—A case study of Dianchi Basin. In *Geoinformatics, 2015 23rd International Conference on* (pp. 1-6). IEEE.

- Chow, A., Li, S., & Fung, A. S. (2016). Modeling urban solar energy with high spatiotemporal resolution: A case study in Toronto, Canada. *International Journal of Green Energy*, 13(11), 1090-1101.
- Coll, C., & Caselles, V. (1997). A split-window algorithm for land surface temperature from advanced very high resolution radiometer data: validation and algorithm comparison. *Journal of Geophysical Research: Atmospheres*, 102(D14), 16697-16713.
- Coll, C., Caselles, V., Valor, E., & Niclòs, R. (2012). Comparison between different sources of atmospheric profiles for land surface temperature retrieval from single channel thermal infrared data. *Remote Sensing of Environment*, 117, 199-210.
- Copiello, S., & Grillenzoni, C. (2017). Solar Photovoltaic Energy and Its Spatial Dependence. *Energy Procedia*, 141, 86-90.
- Díaz, P., Arias, C. A., Peña, R., & Sandoval, D. (2010). FAR from the grid: A rural electrification field study. *Renewable Energy*, 35(12), 2829-2834.
- Er-Raki, S., Chehbouni, A., Hoedjes, J., Ezzahar, J., Duchemin, B., & Jacob, F. (2008). Improvement of FAO-56 method for olive orchards through sequential assimilation of thermal infrared-based estimates of ET. *Agricultural Water Management*, 95(3), 309-321.
- Energy Sage. (2018). What's the best angle for my solar panels? Retrieved from <https://www.energysage.com/solar/101/impact-of-roof-angle/>

- French, A. N., Norman, J. M., & Anderson, M. C. (2003). A simple and fast atmospheric correction for spaceborne remote sensing of surface temperature. *Remote Sensing of Environment*, 87(2-3), 326-333.
- Google Maps. (2018). World Map [website]. Retrieved from <https://www.google.com/maps/>.
- Giauque, W. F., & Stout, J. W. (1936). The Entropy of Water and the Third Law of Thermodynamics. The Heat Capacity of Ice from 15 to 273° K. *Journal of the American Chemical Society*, 58(7), 1144-1150.
- Gillespie, A., Rokugawa, S., Matsunaga, T., Cothren, J. S., Hook, S., & Kahle, A. B. (1998). A temperature and emissivity separation algorithm for Advanced Spaceborne Thermal Emission and Reflection Radiometer (ASTER) images. *IEEE transactions on geoscience and remote sensing*, 36(4), 1113-1126.
- Harris Geospatial Solutions. (2018). Introduction to ENVI LiDAR. Retrieved from http://www.harrisgeospatial.com/docs/using_envi_lidar_Introduction.html
- Kodysh, J. B., Omitaomu, O. A., Bhaduri, B. L., & Neish, B. S. (2013). Methodology for estimating solar potential on multiple building rooftops for photovoltaic systems. *Sustainable Cities and Society*, 8, 31-41.
- Hulley, G. C., Hook, S. J., & Schneider, P. (2011). Optimized split-window coefficients for deriving surface temperatures from inland water bodies. *Remote Sensing of Environment*, 115(12), 3758-3769.

- Jakubiec, J. A., & Reinhart, C. F. (2013). A method for predicting city-wide electricity gains from photovoltaic panels based on LiDAR and GIS data combined with hourly Daysim simulations. *Solar Energy*, 93, 127-143.
- Jiménez-Muñoz, J. C., & Sobrino, J. A. (2003). A generalized single-channel method for retrieving land surface temperature from remote sensing data. *Journal of Geophysical Research: Atmospheres*, 108(D22).
- Jiménez-Muñoz, J. C., Sobrino, J. A., Skoković, D., Mattar, C., & Cristóbal, J. (2014). Land surface temperature retrieval methods from Landsat-8 thermal infrared sensor data. *IEEE Geoscience and Remote Sensing Letters*, 11(10), 1840-1843.
- Kikon, N., Singh, P., Singh, S. K., & Vyas, A. (2016). Assessment of urban heat islands (UHI) of Noida City, India using multi-temporal satellite data. *Sustainable Cities and Society*, 22, 19-28.
- Kodysh, J. B., Omitaomu, O. A., Bhaduri, B. L., & Neish, B. S. (2013). Methodology for estimating solar potential on multiple building rooftops for photovoltaic systems. *Sustainable Cities and Society*, 8, 31-41.
- Labbi, A., & Mokhnache, A. (2015). Derivation of split-window algorithm to retrieve land surface temperature from MSG-1 thermal infrared data. *European Journal of Remote Sensing*, 48(1), 719-742.

- Lahnaoui, A., Stenzel, P., & Linssen, J. (2017). Tilt angle and orientation impact on the techno-economic performance of photovoltaic battery systems. *Energy Procedia*, 105, 4312-4320.
- Liu, L., & Zhang, Y. (2011). Urban heat island analysis using the Landsat TM data and ASTER data: A case study in Hong Kong. *Remote Sensing*, 3(7), 1535-1552.
- Lukač, N., Žlaus, D., Seme, S., Žalik, B., & Štumberger, G. (2013). Rating of roofs' surfaces regarding their solar potential and suitability for PV systems, based on LiDAR data. *Applied energy*, 102, 803-812.
- Mani, M., & Pillai, R. (2010). Impact of dust on solar photovoltaic (PV) performance: Research status, challenges and recommendations. *Renewable and Sustainable Energy Reviews*, 14(9), 3124-3131.
- Mao, K., Qin, Z., Shi, J., & Gong, P. (2005). A practical split-window algorithm for retrieving land-surface temperature from MODIS data. *International Journal of Remote Sensing*, 26(15), 3181-3204.
- Mintz, D. (2009). Technical assistance document for the reporting of daily air quality-the Air Quality Index (AQI). *Tech. Research Triangle Park, US Environmental Protection Agency*.
- National Energy Administration. (2016). The 13th Five-Year Plan for Renewable Energy [可再生能源发展“十三五”规划]. Retrieved from http://www.nea.gov.cn/2016-12/19/c_135916140.htm.

Natural Resources Canada. (2017). About Renewable Energy. Retrieved from <http://www.nrcan.gc.ca/energy/renewable-electricity/7295>.

Paidipati, J., Frantzis, L., Sawyer, H., & Kurrasch, A. (2008). *Rooftop photovoltaics market penetration scenarios* (No. NREL/SR-581-42306). National Renewable Energy Laboratory (NREL), Golden, CO..

Price, J. C. (1983). Estimating surface temperatures from satellite thermal infrared data—A simple formulation for the atmospheric effect. *Remote Sensing of Environment*, 13(4), 353-361.

Schmugge, T., French, A., Ritchie, J. C., Rango, A., & Pelgrum, H. (2002). Temperature and emissivity separation from multispectral thermal infrared observations. *Remote Sensing of Environment*, 79(2-3), 189-198.

Scott, N. A., & Chedin, A. (1981). A fast line-by-line method for atmospheric absorption computations: The Automatized Atmospheric Absorption Atlas. *Journal of Applied Meteorology*, 20(7), 802-812.

Sobrino, J. A., Li, Z. L., Stoll, M. P., & Becker, F. (1996). Multi-channel and multi-angle algorithms for estimating sea and land surface temperature with ATSR data. *International Journal of Remote Sensing*, 17(11), 2089-2114.

Sobrino, J. A., & Jiménez-Muñoz, J. C. (2005). Land surface temperature retrieval from thermal infrared data: An assessment in the context of the Surface Processes and Ecosystem

- Changes Through Response Analysis (SPECTRA) mission. *Journal of Geophysical Research: Atmospheres*, 110(D16).
- Sobrino, J. A., Jiménez-Muñoz, J. C., & Paolini, L. (2004). Land surface temperature retrieval from LANDSAT TM 5. *Remote Sensing of environment*, 90(4), 434-440.
- Sobrino, J. A., Jiménez-Muñoz, J. C., Soria, G., Romaguera, M., Guanter, L., Moreno, J., ... & Martínez, P. (2008). Land surface emissivity retrieval from different VNIR and TIR sensors. *IEEE Transactions on Geoscience and Remote Sensing*, 46(2), 316-327.
- Statler, N. E., Adams, A. M., & Eckmann, T. C. (2017). Optimizing angles of rooftop photovoltaics, ratios of solar to vegetated roof systems, and economic benefits, in Portland, Oregon, USA. *Environment Systems and Decisions*, 37(3), 320-331.
- Stone Jr, B., & Rodgers, M. O. (2001). Urban form and thermal efficiency: how the design of cities influences the urban heat island effect. *Journal of the American Planning Association*, 67(2), 186-198.
- Sun, Q., Tan, J., & Xu, Y. (2010). An ERDAS image processing method for retrieving LST and describing urban heat evolution: a case study in the Pearl River Delta Region in South China. *Environmental Earth Sciences*, 59(5), 1047-1055.
- Tardy, B., Rivalland, V., Huc, M., Hagolle, O., Marcq, S., & Boulet, G. (2016). A software tool for atmospheric correction and surface temperature estimation of Landsat infrared thermal data. *Remote Sensing*, 8(9), 696.

- The City of Vancouver LiDAR [computer file]. (2013). The City of Vancouver, British Columbia. Retrieved from <http://data.vancouver.ca/datacatalogue/LiDAR2013.htm>
- United Nations. (2018). Sustainable Development Goal 7 [website]. Retrieved from <https://sustainabledevelopment.un.org/sdg7>.
- USGS. (2018). Earth Explore [website]. *Science for a Changing World*. Retrieved from: <https://earthexplorer.usgs.gov/>.
- The Green Age. (2018). Impact of orientation, pitch and shading on solar PV. Retrieved from <https://www.thegreenage.co.uk/impact-of-orientation-pitch-and-shading-on-solar-pv/>
- Valor, E., & Caselles, V. (1996). Mapping land surface emissivity from NDVI: Application to European, African, and South American areas. *Remote sensing of Environment*, 57(3), 167-184.
- Wan, Z., & Dozier, J. (1996). A generalized split-window algorithm for retrieving land-surface temperature from space. *IEEE Transactions on geoscience and remote sensing*, 34(4), 892-905.
- World Health Organization [WHO]. (2016). Modelled Global Ambient Air Pollution estimates [website]. Retrieved from http://www.who.int/phe/health_topics/outdoorair/databases/modelled-estimates/en.
- World Weather Online. (2018). Averages [website]. Retrieved from <https://www.worldweatheronline.com/>.

- Xu, H. (2007). Extraction of urban built-up land features from Landsat imagery using a thematic-oriented index combination technique. *Photogrammetric Engineering & Remote Sensing*, 73(12), 1381-1391.
- Yu, X., Guo, X., & Wu, Z. (2014). Land surface temperature retrieval from Landsat 8 TIRS—Comparison between radiative transfer equation-based method, split window algorithm and single channel method. *Remote Sensing*, 6(10), 9829-9852.
- Yale University. (2018). Center for Earth Observation. *Using the MODIS Conversion Tool Kit*.
- Zhang, J., Wang, Y., & Li, Y. (2006). A C++ program for retrieving land surface temperature from the data of Landsat TM/ETM+ band6. *Computers & geosciences*, 32(10), 1796-1805.
- Zhao, L., Tian, Q., Wan, W., Yu, T., Gu, X., & Chen, H. (2010, June). Atmospheric sensitivity on land surface temperature retrieval using single channel thermal infrared remote sensing data: Comparison among models. In *Geoinformatics, 2010 18th International Conference on* (pp. 1-6). IEEE.
- Zhou, B., Zheng, C., & Grigoropoulos, C. P. (2012, June). Optimization of commercial rooftop PV systems in the continental united states using angle-and-wavelength-resolved solar irradiance data. In *Photovoltaic Specialists Conference (PVSC), 2012 38th IEEE* (pp. 002894-002898). IEEE.

